REPORT DOCUMENTATION PAGE

Form Approved OMB NO. 0704-0188

1. REPORT DATE (DD-MM-YYYY)	2. REPORT TYPE	3. DATES COVERED (From - To)
03-03-2015	Final Report	5-Dec-2011 - 4-Dec-2014

4. TITLE AND SUBTITLE	5a. CONTRACT NUMBER
Final Report: Deformation Driven Alloying and Transformation	W911NF-12-1-0010
	5b. GRANT NUMBER
	5c. PROGRAM ELEMENT NUMBER
	611102

6. AUTHORS	5d. PROJECT NUMBER
John H. Perepezko	
	5e. TASK NUMBER
	5f. WORK UNIT NUMBER

7. PERFORMING ORGANIZATION NAMES AND ADDRESSES	8. PERFORMING ORGANIZATION REPORT NUMBER
University of Wisconsin - Madison RESERACH & SPONSORED PROGRAMS 21 N. PARK STREET SUITE 6401 MADISON, WI 53715 -1218	

9. SPONSORING/MONITORING AGENCY NAME(S) AND ADDRESS (ES)	10. SPONSOR/MONITOR'S ACRONYM(S)
U.S. Army Research Office P.O. Box 12211 Research Triangle Park, NC 27709-2211	ARO
	11. SPONSOR/MONITOR'S REPORT NUMBER(S)
	60324-MS.7

12. DISTRIBUTION AVAILIBILITY STATEMENT

Approved for Public Release; Distribution Unlimited

13. SUPPLEMENTARY NOTES

The views, opinions and/or findings contained in this report are those of the author(s) and should not contrued as an official Department of the Army position, policy or decision, unless so designated by other documentation.

14. ABSTRACT

The findings on deformation driven phase reactions in isomorphous systems such as Cu-Ni and Ag-Pd indicate that new kinetic pathways can be exposed that are fundamentally different than those that control conventional thermal annealing where interdiffusion creates a smoothly varying composition profile that leads to a homogeneous solid solution. Under deformation driven interfacial mixing, the composition profile develops an oscillation with an average composition close to the overall multiplayer composition. The amplitude of compositional oscillation decays with further deformation until a uniform solid solution is created. It was also observed that the component

15. SUBJECT TERMS

Deformation Alloying, Mechanochemical Transduction, Multilayer, Driven System

16. SECURITY CLASSIFICATION OF:			17. LIMITATION OF ABSTRACT	15. NUMBER OF PAGES	19a. NAME OF RESPONSIBLE PERSON
a. REPORT	b. ABSTRACT	c. THIS PAGE			John Perepezko
UU	UU	UU	UU		19b. TELEPHONE NUMBER
					608-263-1678

Report Title

Final Report: Deformation Driven Alloying and Transformation

ABSTRACT

The findings on deformation driven phase reactions in isomorphous systems such as Cu-Ni and Ag-Pd indicate
that new kinetic pathways can be exposed that are fundamentally different than those that control conventional thermal annealing where
interdiffusion creates a smoothly varying composition profile that leads to a homogeneous solid solution. Under deformation driven
interfacial mixing, the composition profile develops an oscillation with an average composition close to the overall multiplayer composition.
The amplitude of compositional oscillation decays with further deformation until a uniform solid solution is created. It was also observed
that the component mixing rates during deformation driven mixing are opposite to those that occur during thermal interdiffusion. Further
findings on eutectic systems such as Ni-V and an immiscible system like Cu-Fe also indicate a supersaturated solid solution phase develops
during deformation with the suppression of the nucleation and growth of intermediate phases. In fact, FCC V-rich and BCC Ni-rich solid
solutions in bulk volumes were synthesized by intense deformation. This is a new behavior that has not been reported previously and appears
to be a new feature of mechanochemical transduction. It could also provide new kinetic pathways and the synthesis new microstructures that
cannot be made by conventional thermally activated diffusion. Further study of the underlying mechanisms is warranted.

Enter List of papers submitted or published that acknowledge ARO support from the start of the project to the date of this printing. List the papers, including journal references, in the following categories:

(a) Papers published in peer-reviewed journals (N/A for none)

Received   Paper

TOTAL:

Number of Papers published in peer-reviewed journals:

(b) Papers published in non-peer-reviewed journals (N/A for none)

Received   Paper

TOTAL:

Number of Papers published in non peer-reviewed journals:

(c) Presentations

Non Peer-Reviewed Conference Proceeding publications (other than abstracts):

Received   Paper

TOTAL:

Number of Non Peer-Reviewed Conference Proceeding publications (other than abstracts):

Peer-Reviewed Conference Proceeding publications (other than abstracts):

Received   Paper

TOTAL:

Number of Peer-Reviewed Conference Proceeding publications (other than abstracts):

(d) Manuscripts

Received   Paper

08/28/2014   3.00   Z. Wang, J.H. Perepezko. Interfacial Mixing of Nickel Vanadium Multilayers Induced by Cold Rolling,
Acta Materiala (08 2014)

08/28/2014   4.00   Zhe Wang, John H Perepezko, David Larson, David Reinhard. Mixing Behaviors in Cu/Ni and Ni/V
Multilayers Induced by Cold Rolling,
Journal of Alloys and Compounds (07 2014)

08/29/2013   1.00   Zhe Wang, John H. Perepezko. Deformation-Induced Nanoscale Mixing Reactions in Cu/Ni and Ag/Pd
Multilayers ,
Applied Physics Letters (08 2013)

08/29/2013   2.00   Jörg Neugebauer, John H. Perepezko, Sergej Schuwalow, Marcel H.F. Sluiter, Bo Sundman, Mike W.
Finnis, Albert Glensk, Sergiy Divinski, Jutta Rogal. Perspectives on point defect thermodynamics,
Physica Status Solidi (08 2013)

TOTAL: **4**

Number of Manuscripts:

Books

<u>Received</u>   <u>Book</u>

TOTAL:

<u>Received</u>   <u>Book Chapter</u>

TOTAL:

Patents Submitted

Patents Awarded

Awards

Best Presentation Award -- The Second International Education Forum on Environment and Energy Science, Huntington Beach, California, 2013

First place -- 31st Annual Merrill A. Scheil Metallography Contest, Milwaukee, WI, 2014

Helmholtz Gemeinschaft International Fellow Award (2014)

Graduate Students

NAME	PERCENT_SUPPORTED	Discipline
Zhe Wang	0.50	
FTE Equivalent:	**0.50**	
Total Number:	**1**	

Names of Post Doctorates

NAME	PERCENT_SUPPORTED
FTE Equivalent:	
Total Number:	

Names of Faculty Supported

NAME	PERCENT_SUPPORTED	National Academy Member
John H. Perepezko	0.04	Yes
FTE Equivalent:	**0.04**	
Total Number:	**1**	

Names of Under Graduate students supported

NAME	PERCENT_SUPPORTED	Discipline
Mitchell Dworak	0.20	Materials Science and Engineering
FTE Equivalent:	**0.20**	
Total Number:	**1**	

Student Metrics
This section only applies to graduating undergraduates supported by this agreement in this reporting period

The number of undergraduates funded by this agreement who graduated during this period: 1.00

The number of undergraduates funded by this agreement who graduated during this period with a degree in science, mathematics, engineering, or technology fields:······ 1.00

The number of undergraduates funded by your agreement who graduated during this period and will continue to pursue a graduate or Ph.D. degree in science, mathematics, engineering, or technology fields:······ 1.00

Number of graduating undergraduates who achieved a 3.5 GPA to 4.0 (4.0 max scale):...... 1.00

Number of graduating undergraduates funded by a DoD funded Center of Excellence grant for Education, Research and Engineering:...... 0.00

The number of undergraduates funded by your agreement who graduated during this period and intend to work for the Department of Defense 1.00

The number of undergraduates funded by your agreement who graduated during this period and will receive scholarships or fellowships for further studies in science, mathematics, engineering or technology fields:...... 0.00

Names of Personnel receiving masters degrees

NAME
Total Number:

Names of personnel receiving PHDs

NAME
Total Number:

Names of other research staff

NAME	PERCENT_SUPPORTED
FTE Equivalent:	
Total Number:	

Sub Contractors (DD882)

Inventions (DD882)

Scientific Progress

Technology Transfer

none at this time.

Scientific Progress
Deformation Driven Alloying and Transformation

Table of contents

Executive summary

During intense deformation of multilayers based on different components atomic scale mixing can yield nanoscale alloy synthesis reactions. A systematic investigation is underway to identify the main process and control variable relationships during deformation-induced reactions in specific multilayer pairings. Due to localized interfacial mixing reactions, steep concentration gradients develop that suppress crystal nucleation and allow for the development of metastable states such as supersaturated solutions or amorphous layers. The interfacial mixing reactions are detected by XRD (x-ray diffraction), STEM (scanning transmission electron microscope), APT (atom probe tomography) and calorimetric measurements.

The initial findings on deformation driven phase reactions in isomorphous systems such as Cu-Ni and Ag-Pd indicate that new kinetic pathways can be exposed that are governed by mechanisms that are fundamentally different than those that control conventional thermal annealing where interdiffusion creates a smoothly varying composition profile between the end members (i.e. Cu/Ni and Ag/Pd) that eventually leads to a homogeneous solid solution. Under deformation driven interfacial mixing the composition profile develops an oscillation with an average composition close to the overall multiplayer composition. The amplitude of compositional oscillation decays with further deformation until a uniform solid solution is created. It was also observed that the component mixing rates during deformation driven mixing are opposite to those that occur during thermal interdiffusion. Further findings on the eutectic systems such as Ni-V and an immiscible system like Cu-Fe also indicate a supersaturated solid solution phase develops during deformation with the suppression of the nucleation and growth of intermediate phases. In fact, FCC V-rich and BCC Ni-rich solid solutions were synthesized by intense deformation. This is a new behavior that has not been reported previously and may be a new feature of mechanochemical transduction. It could also provide new kinetic pathways and synthesis new microstructures that cannot be made by thermal activation. Further work is in progress to model the interfacial mixing reactions and phase formation at different strain levels.

Background and Motivation:

One of the highlights of the contemporary attention directed towards nanocrystalline materials is the major innovation in synthesis and processing methodologies that have been developed to achieve nanostructured materials. Within this large and growing menu of options it is possible to characterize the methods into two broad categories: open and closed system processing based upon the manner in which the driving free energy that motivates structural changes is developed during processing.

In a closed system, an energized state is achieved through a rapid temperature, pressure or composition change to create a certain level of undercooling or supersaturation (i.e. a metastable state), which then relaxes towards equilibrium. With an open system, the energized state is often attained by a continuous incremental input to an initial state through the incorporation of excess lattice defects or solute on a localized spatial scale and time interval that is short compared to the relaxation time. During processing, some relaxation is possible and can be expressed by a saturation of stored energy (i.e minimum grain size). With open systems, stable equilibrium phases can be replaced by metastable structures while in closed systems metastable states evolve towards more stable structures. Moreover, the key feature of open

systems is the modification of the kinetic pathways by a continued dynamic input. These systems are also identified as driven systems in the sense that the kinetics are driven by the external input to new pathways and new microstructures that can often be characterized by an effective temperature. The concepts for driven systems were developed initially from the analysis of materials behavior under irradiation, but now the concepts are finding a broader application to materials exposed to intense deformation, wear and deposition processes.

Among the areas that have received longstanding interest is the solid state mixing or mechanical alloying of powder mixtures or multilayers. The basic pattern in the mixing process is a repeated deformation and welding or folding of particles or layers that allows for strain levels in excess of 100 as shown in Fig.1. The deformation of multilayers has a long tradition. While the deformation of multilayer samples has been studied mainly within the context of the mechanics of composites, intense deformation can lead to structural transformations and novel microstructures in multilayer samples.

A precondition for deformation-induced alloying is a mixing reaction at interphase boundaries. In multilayer samples there is now clear evidence that the mixing reactions occur on a nanostructured size scale and yield a true alloying analogous to interdiffusion. However, the nanoscale processes controlling the mixing are more complex that single atom diffusive jumps. The identification of deformation-induced mixing mechanisms is a current focal point of simulation modeling and experimental study. For the deformation driven reactions in samples with a heterogeneous initial structure such as multilayers, several key process parameters have been identified such as the strain, strain rate, deformation temperature, deformation atmosphere and the multilayer stacking architecture.

During the isothermal deformation processing of multilayers, concentration differences exist in the sample that result from localized mixing reactions at the interfaces. The highly localized mixing will yield very steep concentration gradients that act to suppress crystal nucleation. The mixing reactions at the interfaces can be detected based on TEM examination and on the analysis of the X-ray patterns that reflect the alloying with a shift in the peak positions due to lattice parameter changes. Since the foils used for the rolling experiments have an initial thickness of micrometers, the nanoscale thickness of the mixing layer that follows an atomic scale process is small compared with the layer thickness in the initial deformation stage. With continued deformation, the individual layer thickness decreases and therefore the distance between the interfaces decreases. Due to the volume conservation, the interface area increases. The length scale of the bilayer thickness (for binary alloys) and the length scale of the deformation-induced mixing zone at the interfaces, therefore, approach each other and result in complete alloying.

In the current effort, several of the key issues are being addressed including the mechanisms of deformation driven interface mixing, amorphization and devitrification reactions. A key feature of driven systems is the forcing of the kinetics by the external input to new pathways and new microstructures. With model isomorphous systems such as Cu-Ni and Ag-Pd, the progression of alloying with continued deformation can be monitored to evaluate whether defect enhanced diffusion, interface roughening or another process governs the alloying reaction. Over the past year we have completed work on new Cu/Ni multilayer compositions and have advanced the modeling and analysis of the APT results to provide new insight on the interfacial atomic scale mixing process. For completeness some of the results from our prior year report are included in the discussion. With eutectic Ni-V system that has several intermetallic phases, a supersaturated solid solution phase develops during deformation with the suppression of the

nucleation and growth of intermediate phases. FCC V-rich and BCC Ni-rich solid solutions were synthesized by intense deformation, which demonstrates an important feature of mechanochemical transduction. With Cu-Fe immiscible system, a supersaturated solid solution phase was also induced by deformation and a smoothly varying composition profile was revealed from EELS observation. For Ag-Pd system, some equiaxed grains were observed in multilayer sample that initially consisted of columnar grains, which demonstrates that recrystallization was achieved by room temperature rolling. This is a different behavior compared to Cu-Ni, though both systems are considered to be very similar.

Research Progress

Multilayer deformation of isomorphous Cu-Ni

Introduction

Mechanical alloying is a well-established and useful process to fabricate materials with desired properties and synthesize materials in equilibrium and nonequilibrium phases [1-12]. Moreover, it has received increasing attention because it can be utilized to synthesize novel structures which cannot be achieved by thermal activation [13, 14] and it opens a new kinetic pathway to synthesize materials with novel properties [15]. Mechanical alloying has been studied by a variety of methods including cold rolling [16-19], ball milling [20-22], extrusion [23-25], equal channel angular pressing [26-28] and high pressure torsion [29-31]. It has become evident that intense deformation can yield not only nanoscale microstructures, but also induce alloying and phase transformations that are usually considered to be thermally activated. However, the mechanism and the kinetics of mechanical alloying still remain largely unknown [32] compared to the well-established thermodynamic and kinetics analysis for thermally activated reactions. Among the mechanical alloying methods, cold rolling offers some attractions for exploring interfacial mixing. It is a relatively clean technology because as the process progresses, the reactions only happen inside the sample which prevents air from contacting the sample to cause contamination. There is also a dilution of any initial surface contaminants due to the large increase in interfacial area [18].

As a model system Cu/Ni multilayers were investigated because there is complete solubility across the phase diagram [33] without any intermetallic phases or amorphous formation region. Moreover, the Cu-Ni system is a well-established binary system with thermodynamic and kinetic parameters available in the literature, making it possible to compare the transformation and diffusion behavior in driven systems [34, 35] and thermally activated systems.

The isothermal thermally activated diffusion of a Cu/Ni couple has been investigated by low temperature annealing of deposited Cu/Ni multilayers and it was reported that the diffusion concentration profile varies smoothly and continuously [36]. Atom probe tomography (APT) investigation of sputtered Cu/Ni multilayers also shows a smoothly and continuously varying composition between the pure elements upon isothermal annealing [37]. The asymmetry in the

interdiffusion mobility of the two species was revealed by experimental observations that Ni diffuses into Cu faster than Cu diffuses into Ni causing the complete consumption of pure Cu sooner than pure Ni [37]. The same behavior has also been simulated using the Kinetic Monte Carlo method [38]. The interdiffusion coefficients of Ni in Cu [39] and Cu in Ni [40] have been measured and found to be

$$D_{Ni\ in\ Cu} \ = \ 1.95exp(-236.35/RT)\ cm^2 sec^{-1} \qquad (1)$$
$$D_{Cu\ in\ Ni} \ = \ 0.27exp(-255.31/RT)\ cm^2 sec^{-1} \qquad (2)$$

Thus, it is apparent that the diffusion coefficient of Ni in Cu is larger than Cu in Ni at the same temperature. Also, Cu has a lower melting point than Ni indicating the vacancy concentration is larger in the Cu side which enables a larger Ni flux into Cu than Cu into Ni upon isothermal annealing. Since the thermally activated behavior is well established, one challenging question is how the behavior involving phase transformation and mixing occurs under plastic deformation and whether the kinetic pathways and the corresponding mechanism are the same compared to thermal activation. In this work, systematic experiments were performed to investigate the phase transformation and interfacial intermixing behavior of Cu/Ni multilayers subjected to cold rolling.

Experimental Procedure

The initial 25 μm thick Cu and Ni foils with a purity of 99.8% were cut and weighed separately to achieve the average compositions of $Cu_{60}Ni_{40}$ and $Cu_{40}Ni_{60}$ in atomic percent. The foils with desired composition then were stacked alternatively to form the sandwich array as a Cu/Ni/Cu/Ni multilayer structure with 4 initial layers and subjected to cold rolling. The rolling experiments were performed with a hand rolling mill with a roller width of 12.7cm and diameter of 7.6cm. The sample thickness was reduced to a half after it was rolled and it was then folded before the next rolling pass. The time to accomplish one roll is estimated to be 1s. The external input is described using the number of rolling passes, which consists of a roll following by a fold. The structural evolution and the change in lattice parameters at different rolling passes were measured with a Bruker D8 X-ray Diffractometer (XRD) operated with 40kV and 40mA (Cu Kα radiation, step size 0.01 2θ, step time 0.1s). The multilayer spacings and cross-sectional morphology were observed by a LEO 1530-2 scanning electron microscope (SEM) and FEI Titan transmission electron microscope (TEM). The SEM samples were mounted in epoxy, ground down with SiC papers, polished and etched with acetic acid and nitric acid in order to delineate the layers. The TEM samples were prepared by a Zeiss 1540XB crossbeam focused ion beam (FIB) system to investigate the cross-section microstructure. The thin TEM section was achieved by applying 30kV gallium milling at the early stage followed by 5kV milling for final thinning to minimize the gallium contamination and re-deposited materials on the sample cross-section surface. The electron energy loss spectrum (EELS) was measured by the scanning transmission electron microscope (STEM) mode in an FEI Titan TEM with a CEOS probe

aberration-corrector operated at 200keV. The composition profile was determined by analyzing the EEL spectra with Gatan Digital Micrograph software. Atom probe tomography (APT) was performed with a CAMECA local electrode atom probe (LEAP) 4000X HR [41] after 36, 46 and 60 rolling passes. APT samples were prepared with an FEI NOVA 600 Dual Beam FIB with an Omniprobe 200 micromanipulator by lifting out a wedge from the center of the rolled sample, mounting pieces to a series of specimen posts on a microtip coupon, and applying a series of annular mills with the Ga ion beam to produce the necessary radius of curvature at the specimen apex [42]. Specimens were run at a base temperature of 50K, detection rate of 0.50%, laser energy of 50pJ, and a pulse repetition rate of 250kHz.

Results

Upon repeated cold rolling and folding processes, the multilayer thickness was refined and the typical cross-section morphology can be observed by SEM as in Fig. 2. The phase transformation and structural evolution at different rolling passes can be revealed by XRD as shown in Fig. 3. For the $Cu_{60}Ni_{40}$ sample [Fig. 3(a)], initially only individual pure Cu and Ni peaks without any convolution can be observed up to 20 passes. This indicates that a good bonding between the end members has been achieved in the first 20 passes, but there was no significant peak shift or convolution corresponding to mixing. At 25 passes, the Cu and Ni peaks start to convolute with each other causing the valley between the two peaks to rise slightly above the baseline of the diffraction pattern. This indicates that the Cu-Ni solid solution phase starts to form between the end members due to cold rolling. As the deformation level increases, increased Cu/Ni peak convolution, as well as a higher valley between two peaks, can be observed, indicating that the solid solution phase grows and becomes a major phase with increasing deformation. At 55 passes, the Cu peak is no longer detected which indicates that the Cu has been largely consumed while the Ni peak is still detected at the same deformation level. At 60 passes, completion of the transformation reaction has been achieved which is revealed by the observation that both Cu and Ni peaks are not detected and only the Cu-Ni solid solution peaks can be detected in the full range scan. For the $Cu_{40}Ni_{60}$ sample [Fig. 3(b)], a similar trend can be observed, but the intermediate peak position is different. A typical diffraction pattern in the 70°-80° 2θ range and the deconvolution method are illustrated in Fig. 3 in which the two diffraction peaks corresponding to the pure Cu and Ni phases and the convolution peak between the single phase diffraction peaks are revealed using a Lorentz fitting program. The intermediate peak indicates a separate volume of the solid solution phase and the overall diffraction pattern was deconvoluted into three peaks corresponding to pure Cu, solid solution and pure Ni as shown in Fig. 4. The lattice parameters were calculated from deconvoluted peaks by applying the Nelson-Riley Function (NRF) [43] and are shown in Fig. 5 as a function of number of passes [44]. Interestingly, for both compositions the solid solution formed under deformation has the same composition as the average multilayer sample composition and it remains the same with increasing number of rolling passes. The Sherrer formula has been used to calculate the mean thickness of the domain size from the x-ray diffraction peak full width at half maximum intensity

[45] and it was carried out for the layer thickness calculation as shown in Fig. 6. It can be seen through a linear regression fit that Cu and Ni thicknesses decrease in a comparable rate. The cross section microstructure has been examined by TEM and in Fig. 7 it can be observed that the grain morphology is largely elongated with a layer thickness less than 50nm. The STEM EELS measurement reveals the composition across the layer direction in Fig. 8.

From Fig. 8(b) it is evident that the composition profile does not have a continuous variation between pure components but an oscillation in composition is established instead. The statistical average composition can be obtained by the XRD observation in Fig. 5. The cross-section microstructure and composition profile of multilayer samples after 36, 46 and 60 passes were investigated by atom probe tomography. The cross-section view and corresponding composition profile for each sample were generated from the 3-D reconstruction and are shown in Fig. 9-11. From 36 to 46 and 60 rolling passes, more refined multilayer structures are observed in the atom probe cross section views. Moreover, an oscillation in composition of the solid solution is established for every investigated sample. From Fig. 11 it can be seen that after 60 passes, a small amount of Ni still exists however Cu has been consumed. Such a small amount of remaining Ni is not sufficient to contribute to an observable XRD peak.

Discussion
Composition profile and diffusion asymmetry
The XRD results show the peak convolution with increased rolling passes that indicates the formation and development of the solid solution phase. Moreover, when the STEM EELS and atom probe measurements are considered together, it is evident that an oscillation in the composition profile was established due to cold rolling. This response is in contrast to the thermal activation behavior in which the composition profile varies continuously and smoothly from one end member to the other. The other difference between the cold rolling system and the thermally activated system is that under cold rolling, Cu mixes preferentially into Ni rather than Ni mixing into Cu that develops under thermal activation. During the cold rolling the solid solution phase forms and grows with the consumption of single Cu and Ni phases. In the XRD observation for the $Cu_{60}Ni_{40}$ sample at 55 passes, Cu is not detected, meaning that pure Cu has been largely consumed while Ni still exists. This indicates that Cu mixes into Ni preferentially compared to Ni mixing into Cu. This XRD observation is also confirmed by the atom probe result in Fig. 11 which shows that at 60 passes Cu has been consumed but some small amount of Ni still remains. These two differences indicate that the mixing mechanism under cold rolling is fundamentally different from that under thermal activation.

The composition profiles of an Al/Ni multilayer with a negative heat of mixing after repeated folding and rolling [46] and a Cu/Fe multilayer with a positive heat of mixing after high pressure torsion [47] have been reported as continuous variations from atom probe tomography observations. The composition profile of a Cu/Nb multilayer with a positive heat of mixing after accumulative roll bonding and subsequent high pressure torsion was found to have an oscillation shape between the end members [48]. From the results in the present work and in the above reports, it is seen that the deformation induced intermixing kinetics is dependent not only on the

heats of mixing but also on other properties such as deformation behavior of each component [49] and interlayer interface character.

Effective diffusivity

If the mixing were regarded to develop as a result of diffusion, the diffusion length can be estimated by using $x=2\sqrt{Dt}$, where x is the diffusion length, D is the diffusion coefficient and t is the time of the diffusion. From the composition profile obtained from EELS, the thickness of the solid solution, which is 50 nm, can be regarded as the diffusion length x. The solid solution thickness can be observed as 20 nm from the composition profile obtained by atom probe. This local layer thickness variation results from the fact that the strain input is not uniform for each rolling pass which causes a layer thickness variation [50]. Since the two values are on the same order of magnitude, 50 nm was used to calculate the diffusion coefficient under cold rolling. The diffusion time t can be estimated as 36s for 36 rolling passes because the time to accomplish one roll is approximately 1s. Since the room temperature diffusion is negligible, only the time in which the sample was in contact with the roller is considered. After the calculation, the diffusion coefficient can be estimated as 1.7×10^{-17} m^2/s. This high diffusion coefficient cannot be attributed to the thermal activation because if the diffusion is enhanced by a thermal effect due to heating during rolling, the temperature rise could be calculated as up to 1093K according to Eq. 2. This high temperature cannot be achieved since the room temperature rolling mill is massive compared to the sample. The elongated grain structure observed by TEM [Fig. 6] also indicates the mixing is not due to a thermal effect because the grain structure would be expected to be equiaxed after exposure to 1093K. If grain boundary diffusion is considered, the extrapolation of the reported grain boundary diffusivities [51] to room temperature yields values that are still about six orders of magnitude too small to account for the observed mixing.

Effective temperature and deformation induced mixing

The effective temperature concept was first introduced in the irradiation field and indicates that the alloy configuration under irradiation at temperature T is the configuration which would be stable at the temperature T_{eff} in the absence of irradiation [34]. This concept has also been applied in the system under plastic deformation [52, 53] and the effective temperature can be expressed as $T_{eff} = T (1 + \Delta)$, in which $\Delta = D_b/D_t$ where D_b is the ballistic diffusion coefficient and D_t is the thermally activated diffusion coefficient. In driven alloy theory, only a randomly mixed structure is expected due to the assumption that the external deformation leads to random atomic mixing. However, it is found from the static molecular simulations of $A_{50}B_{50}$ alloy systems[54] that binary alloys can mix and demix under an external deformation even at 0 K. This indicates that the atomic motion can be non-random during the driven mixing process. For example, the steady-state atomic configurations of the systems with heats of mixing -90 kJ/mol and 7 kJ/mol are found as chemical ordering and chemical demixing structures, respectively [54]. In order to describe this non-random atomic motion due to the ballistic effect, an intrinsic diffusivity d_b which quantifies the tendency towards equilibrium in the absence of thermal diffusion was introduced and the 'Δ' factor was modified by $\Delta = D_b/(D_t + d_b)$ [54]. A low value of d_b corresponds to a randomizing process and a high value of d_b corresponds to a mixing or

demixing process depending on the value of the heat of mixing. In the present work, the effective temperature is estimated as 1093K at which temperature the diffusion coefficient is of same order of magnitude as that under thermal activation without deformation. The thermally activated diffusion coefficient D_t at room temperature is estimated from Eq. 2 as 5.02×10^{-50} m^2/s. The ballistic diffusion coefficient D_b is estimated from the analysis in the previous section as 1.7×10^{-17} m^2/s. The intrinsic diffusivity in the absence of thermal diffusion d_b is estimated as 6.38×10^{-18} m^2/s. It is seen that the d_b is 32 orders of magnitude larger than D_t, which indicates that the intermixing is preferred and is attributed to the ballistic effect due to cold rolling rather than thermal activation. In a prior work of $Ni_{70}V_{30}$ multilayers subjected to cold rolling [55], the d_b is estimated as 6.8×10^{-18} m^2/s, which is of same order of magnitude as the value in this work, and the intermixing of Ni and V has been observed. However, an oscillation is established in the composition profile of $Cu_{60}Ni_{40}$, but an oscillation is not established in the composition profile of $Ni_{70}V_{30}$ as-rolled sample [56]. This indicates that although the ordered steady-state configurations are related to the large values of d_b, how the atoms evolve towards to the static equilibrium varies among systems.

Transformation kinetics

The transformation kinetics can be illustrated by examining the layer thickness distribution. The layer thickness follows a log-normal distribution and the fraction of reaction completed can be expressed as the integration of the log-normal distribution from 0 to a threshold value as shown in Eq. 3, where f is the fraction of sample that has transformed into the solid solution phase, t is the layer thickness, n is the rolling passes, $\mu(n)$ is the log-mean and $\sigma(n)$ is the log-variance of the distribution respectively.

$$f = \int_0^{Threshold} \frac{1}{\sqrt{2\pi}\sigma(n) \cdot t} \exp\left(-\frac{(\ln t - \mu(n))^2}{2\sigma(n)^2}\right) \qquad (3)$$

Since the integration of the log-normal distribution is an error function, the transformation kinetics is described by using an error function representation in Eq. 4, in which A, B are the fitting parameters. A and B can be found by fitting Eq. 4 to experimental data as 0.08 and -37.5 respectively.

$$f = 0.5[1 + Erf(A*(n+B))] \qquad (4)$$

The parameter B reflects the translational shift from zero position to enter the range of passes where the reaction occurs. It also indicates the number of passes needed to transform half of the sample into a solid solution. The parameter A reflects the reaction rate of the binary system in which a larger A leads to a steeper slope of the error function curve which further indicates a higher intermixing rate.

After the integration of Eq. 3, the fraction can be expressed, where C is the integration constant, by:

$$f = \frac{1}{2} + \frac{1}{2} erf\left(\frac{\ln t \big|_0^{Threshold} - \mu(n)}{\sqrt{2}\sigma(n)}\right) = \frac{1}{2} + \frac{1}{2} erf\left(\frac{C - \mu(n)}{\sqrt{2}\sigma(n)}\right) \qquad (5)$$

By comparing the Eq. 4 and Eq. 5, the log-mean follows the relationship $\mu(n) = 53.4/n$ and log-variance follows $\sigma(n) = 12.6/n$. The details of the layer thickness distribution and the corresponding statistical analysis are given in Appendix 1. The mixing layers per rolling pass, l_{mix}, can be expressed as

$$l_{mix} = 396697 * \frac{df}{dn} = 22443 * \exp(-(0.08n - 3)^2) \tag{6}$$

which is illustrated as in Fig. 11. The details about the derivation of Eq. 6 are shown in Appendix 1. From Fig. 11 it can be seen that the mixing layers per pass is not the same for each pass. At the beginning and the end of the reaction, the number of mixing monolayers is small. In the middle of the reaction the number of mixing monolayers becomes large.

Evolution of solid solution formation

A characteristic transformation behavior induced by cold rolling of the Cu/Ni multilayer is the establishment of an oscillation in composition between pure components, which represents a form of an alternative Cu-rich/Ni-rich structure in the solid solution regime. For each APT sample, the composition profiles were surveyed across the multilayer direction from five individual regions. The oscillation can be observed in each composition profile. As a simplified representation the profile is fitted by a sinusoid model. The amplitude ranges are shown in Fig. 12(a) as a form of box plots [57], in which the variation is due to different local areas at the same deformation level. The baselines are shown in Fig. 12(b) and reveal a slowly varying trend to approach the average sample composition. This indicates the average composition of solid solution phase remains close to the nominal sample composition with increased deformation, which is consistent with the XRD measurements. With increased deformation, the amplitude will eventually decay to zero, which indicates that the homogeneous solid solution phase with a composition the same as average sample composition will be achieved after sufficient deformation.

Conclusion

Upon repeated rolling and folding, the layer thickness of a multilayer Cu/Ni sample can be dramatically refined down to the nanoscale. The mixing behavior induced by cold rolling was investigated and it was found that an oscillation in composition is established between the end members due to cold rolling, which is in contrast to thermally activated diffusion. The composition oscillation in the solid solution phase is described by a simplified sinusoid model in which the amplitude decays with increased deformation. In contrast to the expected thermally activated diffusion behavior, during cold rolling Cu is observed to mix into Ni preferentially compared to Ni mixing into Cu. The effective diffusion coefficient was calculated as 1.7×10^{-17} m^2/s which cannot be attributed to thermal activation. The effective temperature is estimated as 1093K. The largely promoted diffusion coefficient could be related to the effective temperature concept, but the establishment of an oscillation in the composition profile is a specific behavior that is due to deformation.

Multilayer deformation of eutectic system Ni-V

In prior work, the extent and character of the interfacial mixing was examined during deformation of multilayers in the isomorphous Cu-Ni system [44]. As a next step in the systematic study of deformation induced interfacial reactions, the Ni-V system was selected since the end members have different crystal structures and there are several intermediate alloy phases. In addition there is thermodynamic and kinetic data available for the analysis of the structural evolution during intense deformation.

Experimental methods

The 25 μm thick Ni and V elemental foils with a purity of 99.8% were cut and weighed separately to achieve the average compositions $Ni_{70}V_{30}$, $Ni_{30}V_{70}$ and $Ni_{57}V_{43}$ in atomic percent. Then, the Ni and V foils were stacked alternatively to form the sandwich array as a Ni/V/Ni/V structure with different initial areal size to achieve the desired composition. The cold rolling experiments were performed with a hand rolling mill. The time to accomplish a roll is estimated as 1s and the multilayer foil was folded in half after each roll that reduced the sample thickness by 50%. The deformation level was described by the number of passes in which one pass consists of a roll and a fold. With the folding operation after each rolling pass no new reaction interfaces are created and all existing reaction interfaces experience the same number of passes. The phase transformation and structural evolution were monitored with a Bruker D8 Advance X-ray Diffractometer (XRD). The microstructure was examined with Zeiss LEO 1530-2 scanning electron microscope (SEM) and FEI Titan scanning transmission electron microscope (STEM) with a CEOS probe aberration corrector. The composition was analyzed from the electron energy loss spectrum (EELS) using the Gatan Digital Micrograph software. The STEM samples were prepared by Zeiss 1540XB cross beam focused ion beam (FIB) system with 30kv milling followed by a 5kv cleaning as the final step to minimize the surface contamination.

Results and discussions

Evolution of solid solution formation and composition profile

The XRD pattern for the as-rolled $Ni_{70}V_{30}$ multilayer sample after different passes can be monitored as in Fig. 14(a). During the initial 15-30 passes, only individual peaks corresponding to pure FCC Ni and BCC V appear in the XRD pattern. Above 35 passes, in the 40°-50° 2θ range the Ni and V peaks start to convolute into each other which indicates the formation of a solid solution between the single phases. At 50 passes, an intermediate peak appears which indicates the solid solution phase becomes a major component in the sample. At 80 passes, the Ni and V peaks completely merge into one single peak which means the Ni and V single phases completely transform into the solid solution phase. The lattice parameters corresponding to Ni, V and solid solution phase with an average composition at different rolling passes are shown in Fig. 14(b). It is seen that both Ni and V have been consumed within 5 addition passes from 75 to 80 passes. No significant change of XRD patterns was observed from 80 to 90 passes. At 90 passes,

the crystal structure of the solid solution was determined as FCC from the positions of diffraction peaks. From the evolution of the diffraction patterns, no significant change of Ni and V peak positions was observed when the pure Ni and V layers remain in the sample. It is also noted that since the FCC Ni has a lattice constant 0.352 nm [58] and BCC V has a lattice constant 0.304 nm [59], the solid solution phase has a larger lattice constant than pure Ni and the corresponding diffraction peak will shift to the smaller angle side compared to Ni peak according to Bragg's law [60]. This trend is shown for the Ni (200) peak around 50° and high angle peaks between 70°-80°. If vanadium is assumed to be FCC, the corresponding lattice parameter is calculated from the hard sphere atom size of BCC is 0.372 nm. It is seen that the lattice parameter of the FCC solid solution is between that of FCC Ni and FCC vanadium. If the Vegard's law [61] is applied on FCC Ni and FCC vanadium, the lattice parameter of the FCC solid solution is estimated as 0.358 nm for the $Ni_{70}V_{30}$ composition, which is very close to the XRD measured value that is 0.359 nm.

The XRD pattern for the as-rolled $Ni_{30}V_{70}$ multilayer sample after different passes can be monitored as in Fig. 15(a). It is seen that initially only FCC Ni and BCC V peaks appear in the XRD pattern. With further deformation, a solid solution forms and becomes a major component in a similar way as for the $Ni_{70}V_{30}$ sample. After 90 passes the Ni and V peaks completely merge into one single peak which indicates that the Ni and V pure components completely transform into the solid solution phase. In contrast to $Ni_{70}V_{30}$ sample, the crystal structure of the solid solution in $Ni_{30}V_{70}$ sample is determined as BCC from the positions of diffraction peaks. If nickel is assumed to be BCC, the corresponding lattice parameter is calculated from that of FCC Ni as 0.287 nm. This indicates that the lattice parameter of BCC solid solution phase is smaller than that of vanadium and the corresponding diffraction peak position will shift to the larger angle side compared to V peak. This trend is seen in Fig. 2(a) for V (200) peak between 60°-65° and V (211) peak between 75°-80°. The lattice parameters corresponding to Ni, V and solid solution phase with an average composition at different rolling passes are shown in Fig. 15(b). It is seen that the lattice parameter of BCC solid solution is between that of BCC Ni and BCC vanadium. If the Vegard's law [61] is applied on BCC Ni and BCC vanadium, the lattice parameter of the BCC solid solution is estimated as 0.299 nm for the $Ni_{30}V_{70}$ composition. It is seen that the XRD measured value which is 0.296nm is in a good agreement with the estimated value from Vegard's law.

The XRD pattern for the as-rolled $Ni_{53}V_{47}$ multilayer sample after different passes can be monitored as in Fig. 16(a). It is seen that initially only FCC Ni and BCC V peaks appear in the XRD pattern. Different from $Ni_{70}V_{30}$ or $Ni_{30}V_{70}$, both FCC and BCC solid solutions form upon further deformation. After 90 rolling passes the Ni (111) and V (110) diffraction peaks completely merge into one single peak which indicates that the Ni and V pure components completely transform into solid solution phases. The XRD pattern of $Ni_{53}V_{47}$ multilayer after 100 rolling passes [Fig. 16(b)] shows both FCC and BCC diffraction peaks. If the Vegard's law [61] is applied on FCC Ni and FCC vanadium, the lattice parameter of the FCC solid solution is estimated as 0.361 nm for the $Ni_{53}V_{47}$ composition. From the application of Vegard's law [61] to

BCC Ni and BCC vanadium, the lattice parameter of the BCC solid solution is estimated as 0.295 nm for the $Ni_{57}V_{43}$ composition. It is seen in Fig. 16(c) that in both cases the XRD measured values are in good agreement with the estimated values from Vegard's law.

It is noted that the X-ray diffraction provides the macroscopic statistical average composition of the solid solution. However, the local composition at nanometer scale in the solid solution region can be variable. For example, in our previous investigation of Cu/Ni multilayers subjected to cold rolling [44,56], the solid solution peak in the XRD pattern appears at the position that corresponds to the solid solution with a nominal composition, i.e. Cu60Ni40. The compositional information that is obtained from STEM EELS shows that the local composition in the Cu-Ni solid solution region is variable where some local regions are Cu-rich and some are Ni-rich. In this work, the local compositions in the Ni-V solid solution region are also observed to be variable.

The SEM images of $Ni_{51}V_{49}$ multilayer cross-sections after 30 rolling passes are shown in Fig. 17. It is seen that the layers have irregular shapes with non-uniform layer thicknesses. In order to investigate the microstructure and composition profile of the multilayer sample, STEM EELS was conducted on the $Ni_{70}V_{30}$ sample after 60 passes where the solid solution coexists with pure Ni and V. Fig. 18(a) shows the multilayer microstructure where the white layer corresponds to Ni and black layer corresponds to V. The layer between white and black layers that has lower contrast than the white layer is the solid solution phase and its composition profile can be obtained by EELS analysis. It is evident from Fig. 18(a) that the layer thickness was refined to about 30nm for Ni and about 10nm for V. Since every pixel in the EELS image has the spectrum information, the composition can be obtained by quantifying the EELS edges and the profile as shown in Fig. 18(b). It can be noticed that the profile between Ni and V varies smoothly and continuously from one end member to the other without evidence for the formation of any of the intermediate phases that are present in the equilibrium phase diagram shown in Fig. 19.

Effective diffusion coefficients

Since the diffusion coefficients calculated through the Boltzmann-Matano [62] method for compositions near the limiting values are subject to considerable uncertainty [63], an alternative analytical method suggested by Hall [63] that improves the accuracy near the extremes of the composition range was used to calculate the effective diffusion coefficients. The simplified expression deduced by Crank [64] is shown in the Eq. 7, where u is the probability of Ni mole fraction C and it is given by the Eq. 8.

$$D(C) = \frac{1}{h^2} + k\frac{\pi^{\frac{1}{2}}}{h^2}(1+erf(u))\exp(u^2) \tag{7}$$

$$\frac{1}{2}(1+erf(u)) = C \tag{8}$$

$$C = \frac{1}{2}[1 + erf[-0.51*(X-4.64)]]$$
(9)

In Eq. 7, h and k are the slope and intercept in the plot of u against $X/t^{1/2}$, where X and t are the diffusion distance and time, that can be determined from the linear regression of the plot in Fig. 20(a). The composition profile of $Ni_{70}V_{30}$ multilayer sample from the 85nm-94nm range in Fig. 18(b) was fitted with an error function and the composition C and distance X values used to calculate u and D(C) are from the fitting. The calculated composition dependent diffusion coefficient is shown in Fig. 20(b).

When the measurements by XRD and STEM EELS are combined, it is evident that the transformation from Ni and V single phases to a solid solution phase occurs during cold rolling with suppression of nucleation of intermetallic phases in the phase diagram. From Fig. 20(b), the diffusion coefficient varies from $1.2 \times 10^{-15} cm^2/s$ to $1.6 \times 10^{-13} cm^2/s$ according to different compositions. In the thermal activation process, the diffusion coefficient can be expressed as in Eq. 10. From the measurement of average interdiffusion coefficient due to thermal activation by Davin [16] et al, D_0 is determined as $0.287 cm^2/s$ and ΔH is determined as 248kJ/mol.

$$D = D_0 \exp(-\frac{\Delta H}{RT})$$
(10)

If Eq. 10 is applied, the room temperature diffusion coefficient can be calculated as 1.02×10^{-44} cm^2/s. This comparison implies that the effective diffusion coefficient induced by deformation can be enhanced by about 30 orders of magnitude compared to the diffusivity due to thermal diffusion. Similar large enhancements of an effective diffusivity have also been reported elsewhere such as a promotion of 22 orders of magnitude in Cu-Co alloys by high pressure torsion [66]. If this promoted diffusion coefficient is considered as a thermal activation effect, the corresponding effective temperature can be calculated from Eq. 10 as 900K to 1057K. Such a high temperature cannot be achieved during cold rolling since the rollers are massive compared to the sample. This indicates that the accelerated diffusion is attributed to the deformation induced atomic mixing process rather than to any thermal effect. It has been reported that the binary alloy can mix under an external driving force at 0K from the Monte Carlo simulation work [54], which supports the point that the accelerated diffusion is achieved due to deformation instead of thermal assistance. It can be seen from the STEM image [Fig. 18(a)] that Ni layers have a larger layer thickness than the V layers. The statistics of the Ni and V layer thickness was studied from different STEM images and the distribution was revealed to follow the log-normal distribution in which Ni-rich layer thickness has a larger mean value than the V-rich layer [Fig. 21]. Since the initial thickness is the same 25μm for both Ni and V, it is apparent that Ni mixes into V preferentially compared to V mixing into Ni. This is also supported by the effective interdiffusion coefficient variation with composition [Fig. 20(b)]. Initially only single Ni and V phases exist in the multilayer. Nickel mixes into the V side and V mixes into the Ni side in response to cold rolling [Fig. 20(c)]. As the solid solution forms between the single phases, the

14

interlayer mixing is greater for every position at Ni-rich side compared to the corresponding position which is symmetric to the interface at the V-rich side. Since the flux is larger for the Ni mixing direction [Arrow 1 in Fig. 20(c)] than for the V mixing direction [Arrow 2 in Fig. 20(c)] across the interface, this results in consumption of V before Ni during deformation. From Fig. 18(b) the evidence that no local Ni consumption can be observed, but V local consumption can be observed at the 25 nm and the 55nm position is consistent with and supports the above analysis.

The thermal activation induced composition dependent interdiffusion coefficient of Ni and V has been reported by Million [67]. In the 0-40 at. % V composition range, the diffusion coefficients for both Ni and V decrease with the increasing V composition in the range of 0-22 at. % V and increase with increasing V composition in the range of 22-40 at. % V. The deformation induced diffusion coefficient shown as in Fig. 20(b) has a monotonically increasing variation with increasing Ni composition in the 0-40 at. % V range without a minimum point occurring at 22 at. % V composition. This indicates that the trend of interdiffusion coefficient variation against composition is different compared to the thermally activated behavior.

Phase selection and suppression

The solid solution is identified as an FCC structure in the $Ni_{70}V_{30}$ multilayer sample for the entire composition range at 60 passes since at this deformation level only peaks corresponding to FCC solid solution phase, but no peak corresponding to BCC solid solution phase can be observed in the XRD pattern even though the intermixed zone spans V-rich compositions that would be expected to have a BCC structure. In order to understand this result, the metastable Ni-V phase diagram in the absence of intermediate phases was calculated as shown in Fig. 19. The Gibbs energies of the solid solution phases and liquid phase were expressed in the form given by

$$G^{\phi} = C *{}^0 G_{Ni}^{\phi} + (1-C) *{}^0 G_V^{\phi} + RT(C*\ln C + (1-C)*\ln(1-C)) + C*(1-C)*\sum_{i=0}^{n} {}^i L*(2C-1)^i \quad (11)$$

where C is Ni mole fraction, ${}^0 G_{Ni}^{\phi}$ and ${}^0 G_v^{\phi}$, where ϕ stands for FCC, BCC and liquid phases, are the Gibbs energies for pure Ni and V at the reference state at 298.15K. The data for the Gibbs energies for pure components were taken from Dinsdale [68]. The L parameters for each phase are determined from the compound energy formalism (CEF) model [69] where the σ phase is treated as $(Ni,V)_{18}(V)_4(Ni)_8$. The Ni_2V, Ni_3V and Ni_2V_7 phases are treated as line compounds. In addition, the T_o temperature, at which the solid solution phase and liquid phase have a same Gibbs energy at a given composition, was calculated for BCC/liquid and FCC/liquid in order to determine if FCC phase is stable at the estimated effective temperature. From Fig. 22 it is evident that the metastable diagram yields a eutectic between the FCC and BCC solid solutions and the liquid. The FCC solid solution is more stable (i.e. it has a higher T_o temperature) than the BCC solid solution up to the crossing point of the T_o(BCC/L) and T_o(FCC/L) curves at 42 at.% Ni. For V compositions greater than 42 at.% Ni the BCC solid solution is more stable than the FCC solid solution, but a complete FCC solid solution can still develop over the entire composition range by the addition of excess chemical free energy. In the absence of the BCC solid solution the metastable Ni-V diagram becomes an isomorphous system as shown by the extended liquidus

and solidus phase boundaries in Fig. 22. For the $Ni_{30}V_{70}$ multilayer sample, the solid solution phase is identified as BCC structure at the deformation stages where the solid solution coexists with pure Ni and V components. Though the intermixed zone spans Ni-rich compositions that would be expected to have FCC structures since FCC solid solution is more stable for Ni compositions greater than 42 at.%Ni, the BCC solid solution can still be achieved by the addition of excess chemical free energy. Similarly, in the absence of the FCC solid solution the metastable Ni-V diagram also becomes an isomorphous system as shown by the extended liquidus and solidus phase boundaries in Fig. 22.

A further enhanced level of chemical free energy is derived from the FCC structure that is associated with the concentration gradient in Fig. 18. For V-rich alloy with V compositions greater than 42 at. % Ni, a BCC phase should develop according to the metastable phase diagram [Fig. 22]. However, when the FCC phase is present instead of the BCC phase at C=0.1, there is an additional free energy increase of 4.59 kJ/mol that is noted as ΔG_2 in Fig. 23. For pure vanadium, the FCC structure can also be achieved from BCC vanadium by additional energy input 8.00kJ/mol that is noted as ΔG_1 in Fig. 23.

Since the multilayers of different alloy compositions have the same end members (i.e. Ni and V), the layer refinement and mixing behavior in $Ni_{30}V_{70}$ multilayer sample upon deformation should be similar compared to $Ni_{70}V_{30}$. It is seen from XRD pattern that a BCC Ni-rich solid solution was induced starting at about 35 passes. This could also be achieved by the addition of excess chemical free energy from deformation. It is seen from Fig. 23 that at Ni mole fraction 0.9, FCC solid solution can be transformed to BCC by an additional energy input of 6.45kJ/mol that is noted as ΔG_3. FCC Ni can also be transformed into BCC Ni by additional energy input of 7.36kJ/mol that is noted as ΔG_4. Usually metastable BCC nickel can be achieved in thin films by hetero-epitaxial growth during deposition but it transforms into stable FCC structure when film thickness increases [70, 71]. For example, BCC nickel can be achieved by epitaxial growth on an Fe (001) substrate up to 6 monolayers before the transformation occurs [72]. In the present work it is demonstrated that metastable BCC solid solution can be achieved in a bulk form in the absence of thermal activation by additional energy input through the cold rolling process.

Shear mixing and mixing kinetics

The intermixing observed in the present work is considered as a chemical mixing process induced by deformation instead of by thermally activated processes because the physical temperature is not enough to promote a large vacancy migration rate. In fact, the temperature rise in the high pressure torsion, which is a more severe deformation process than rolling, is also too low to account for the initiation of solid state reaction [73]. The mechanism of deformation induced chemical mixing has been examined by molecular dynamic simulations of Cu heterogeneous systems containing precipitates and other model systems [74, 75]. The findings reveal that low temperature shear mixing is attributed to the dislocation glide in all their studied systems and the mixing behavior depends on the type of interface [74]. For the coherent interfaces, shear induced mixing is achieved by dislocations transferring across the phase boundaries and for the incoherent precipitate interfaces, mixing is achieved by a local shuffling

of atoms at the interface [75]. In the Ni-V multilayer system, incoherent interfaces are expected between Ni and V layers because of their different crystalline structures thus the intermixing is likely to be attributed to a local atomic shuffling effect. Moreover, the deformation is expected to induce rough interfaces as noted in Fig. 17 [76, 77], which will assist the atomic shuffling to occur. Another factor that plays an important role in the low temperature deformation driven mixing process is the heat of mixing, since it is related to the local energy barrier during relaxation [74, 75]. In the static molecular simulation work on $A_{50}B_{50}$ alloy systems under external mechanical alloying at temperature 0K [54], it was found that the system with a heat of mixing -22kJ/mol evolves towards a more short-range ordered structure from a segregated structure as the time of mechanical alloying increases. Since Ni and V have a heat of mixing -18kJ/mol at the equiatomic composition [78], the observed intermixing is in accord with the simulation results.

The formation of metastable solid solutions induced by mechanical alloying has been studied on a variety of systems such as Ti-Al [79], Al-Cu [80], Al-Fe [81], Fe-Co [82], and Fe-Pd [83]. Even in the systems with a positive heat of mixing such as Al-Zn [84], Cu-Co [8], Ag-Cu [85] and Ag-Ni [86], the formation of supersaturated solid solution has been reported. Moreover, the overlapping of solid solubility where the FCC and BCC solid solutions have a same composition has been observed in the mechanical alloyed Cu-Fe and Fe-Ni [87]. Although the mechanical alloying induced solid solution formation has been extensively studied, the mixing kinetics, i. e. how the end members intermix before the solid state reaction achieves a completion, is still unclear and the composition profiles induced by mechanical alloying are only available for a few systems. The composition profiles of Al/Ni multilayer after repeated folding and rolling [88] and Cu/Fe after high pressure torsion [89] have been reported as a continuous variation from the atom probe tomography observations. The composition profile of Cu/Nb multilayer after accumulative roll bonding and subsequent high pressure torsion was found to have an oscillation shape between the end members [48]. In previous work [44,56], the composition profile of Cu-Ni multilayer after cold rolling was found to be oscillating in the mixing zone between pure Cu and Ni. The above investigations on intermixing behavior induced by mechanical alloying indicate that although the solid solutions were eventually achieved as a consequence of external deformation, the kinetics vary among different systems. Cu-Fe and Cu-Nb have certain similarities since they are both FCC/BCC crystalline structures with a positive heat of mixing (+13kJ/mol for Cu-Fe and +3kJ/mol for Cu-Nb at equiatomic composition [78]), however their mixing profile unexpectedly differs. Ni-V and Cu-Fe have a negative and positive heat of mixing respectively but the shape of their composition profiles is similar. This indicates that mixing kinetics doesn't depend only on the heat of mixing and it is related to other factors such as the deformation behavior of each component and the interlayer interface character.

Mechanochemical transduction

Usually mechanochemical transduction is considered to be related to deformation inducing contact between components to promote a chemical reaction or to induce morphology changes in organic systems with extended chain molecular structures [90-92]. However, another form of

mechanochemical transduction is demonstrated in this study by the storage of a portion of the deformation work as excess chemical free energy that can activate a material for subsequent reaction. The overall stored energy from deformation can be estimated as the sum of dislocation energy, chemical energy and interfacial energy. The dislocation energy is estimated from [93].

$$E_{Disl} = \frac{Gb^2}{4\pi} \ln(\frac{R}{r_o}) \rho_D V_m \tag{12}$$

In Eq. 12, the Burgers vector b can be estimated as 0.253 nm for $Ni_{70}V_{30}$ and 0.259 nm for $Ni_{30}V_{70}$ by applying the relationship $|b| = \frac{a}{\sqrt{2}}$ for FCC systems and $|b| = \frac{\sqrt{3}a}{2}$ for BCC systems. The dislocation separation R is estimated as 10 nm for a dislocation density of 10^{12} cm^{-2} that is representative for a heavily cold worked metal. The shear modulus of pure Ni, which is 76 GPa, is applied for the estimation for $Ni_{70}V_{30}$ sample and shear modulus of pure V, which is 47 GPa, is applied for the estimation for $Ni_{30}V_{70}$ sample. The sample molar volumes of $Ni_{70}V_{30}$ and $Ni_{30}V_{70}$ are estimated as 7.0 cm^3/mol and 7.8 cm^3/mol respectively. The dislocation core radius, r_o is assumed as 3b. By substituting all the parameters into Eq. 12, the dislocation energies are estimated as 70 J/mol for $Ni_{70}V_{30}$ and 50 J/mol for $Ni_{30}V_{70}$. The chemical free energies are estimated from the energy difference between FCC and BCC solid solution phases and they are found to depend on compositions as shown in Fig. 23. The chemical free energies are 4.59 kJ/mol for Ni mole fraction 0.1 and 6.45 kJ/mol for Ni mole fraction 0.9. The interfacial energy can be estimated by:

$$E_{int} = S_v \gamma_{gb} V_m \tag{13}$$

In Eq. 13, S_v is the interfacial area per volume and it is estimated as 7.9×10^7/m for $Ni_{70}V_{30}$ sample by counting the numbers of intersections between the interfaces and a test line with a known distance that is across the multilayers in STEM images. The grain boundary energy for pure Ni is estimated as 1J/m^2 [94]. The stored interfacial energy for $Ni_{70}V_{30}$ sample is estimated from Eq. 13 as 553 J/mol. Since the layer refinement of $Ni_{30}V_{70}$ sample is similar as $Ni_{70}V_{30}$ sample, the stored S_v for $Ni_{30}V_{70}$ sample is estimated to be the same as that for $Ni_{70}V_{30}$ sample and the interfacial energy for $Ni_{30}V_{70}$ sample is estimated as 616J/mol. For both $Ni_{70}V_{30}$ and $Ni_{30}V_{70}$ multilayer samples, compared to the stored energy due to dislocation or interfaces, the chemical free energy is the largest portion of the total stored energy from deformation work. This represents a form of mechanochemical transduction.

The Gibbs energies of liquid, FCC and BCC phases at room temperature are shown in Fig. 24(a). The Gibbs energy difference between liquid and FCC phases, $\Delta G^{Liquid/FCC}$ is shown in Fig. 24(b) and the Gibbs energy difference between liquid and BCC phases, $\Delta G^{Liquid/BCC}$ is shown in Fig. 24(c). It is seen from Fig. 24(b) that the minimum $\Delta G^{Liquid/FCC}$ is 8.76kJ/mol at Ni mole fraction 0.5, which indicates that the minimum Gibbs energy required to transform FCC phase to liquid is 8.76kJ/mol. For $Ni_{70}V_{30}$ sample at a Ni mole fraction 0.1, 10.36kJ/mol energy is required to transform FCC to liquid phase. However, the total stored energy on FCC solid

solution from deformation as the sum of dislocation energy and interfacial energy is estimated as 0.62kJ/mol. Since the total stored energy on FCC solid solution is significantly smaller than $\Delta G^{Liquid/FCC}$, the amorphous phase is not expected to form from FCC solid solution based on thermodynamic predication, which is consistent to the fact that no amorphous phase was observed in the $Ni_{70}V_{30}$ sample. For $Ni_{30}V_{70}$ sample at Ni mole fraction 0.9, the total stored energy on BCC solid solution as the sum of dislocation energy and interfacial energy is estimated as 0.67 kJ/mol. The energy required to transform BCC solid solution to liquid at Ni mole fraction 0.9 is 6.12 kJ/mol. The total stored energy on BCC solid solution is again significantly smaller than $\Delta G^{Liquid/BCC}$, which indicates that the amorphous phase is not expected to develop from the BCC solid solution in $Ni_{30}V_{70}$ sample. The overview of energy levels for $Ni_{70}V_{30}$ sample at Ni fraction 0.1 and $Ni_{30}V_{70}$ sample at Ni fraction 0.9 are shown in Fig. 25 and 26. It is interesting to note that for the $Ni_{57}V_{43}$ sample both metastable BCC and FCC solid solutions develop after complete transformation even though, as indicated in Fig. 24, the Gibbs energy for the BCC solution is 2.74 kJ/mol larger than that for the FCC solid solution.

Conclusion

In conclusion, the solid solution phase transformation of $Ni_{70}V_{30}$ and $Ni_{30}V_{70}$ multilayers resulting from the deformation induced interlayer mixing was observed to yield a composition profile that varies smoothly and continuously from one end member to the other. Based upon the observed deformation induced mixing, the effective interdiffusion coefficient was promoted by about 30 orders of magnitude compared to thermal activation and it increases monotonically with the increase of Ni mole fraction. It was also found that Ni mixes into V preferentially. With continued rolling the layer refinement eventually leads to an overlap of the interlayer mixing zones and complete transformation. With the addition of excess chemical free energy input from cold rolling in the $Ni_{70}V_{30}$ multilayer metastable FCC solid solutions were induced and in the $Ni_{30}V_{70}$ multilayer metastable BCC solid solutions were induced while in the $Ni_{57}V_{43}$ multilayer complete transformation yielded a duplex product of metastable BCC and FCC solid solutions. Another form of mechanochemical transduction is demonstrated in this study by the storage of excess chemical free energy as a large portion of total stored energy from deformation. The deformation induced synthesis of bulk metastable BCC and FCC solid solutions offers new opportunities for applications.

Multilayer deformation of immiscible system Cu-Fe

Mechanical alloying (MA) has become a longstanding interest due to its practical simplicity to produce alloys with desired properties and applications. Cu-Fe, as one of the immiscible systems with positive heat of mixing, has drawn great attention because of the magnetic properties of its solid solution [95]. The possibility to form unstable solid solution Cu-Fe by means of MA has been confirmed in varieties of studies [96-99]. With further efforts, the extension of solid solubility has been reported [100, 101] and the overlapping of solid solution has been revealed [102-104] that single FCC alloys of Fe_xCu_{1-x} ($x \leq 60$), single BCC alloys ($x \geq 80$) and FCC-BCC two phase coexistence ($60 \leq x \leq 80$) can be formed by MA. Even though a better understanding

in the Cu-Fe solid state reaction has been achieved from previous researches, details in the kinetic pathway towards the formation of solid solution, i. e. how the intermixing is induced by deformation before the completion of solid state reaction, is still unclear. In the present study, cold rolling induced intermixing in Cu-Fe multilayers was investigated. Cold rolling method was chosen because on one hand it has an advantage to study the kinetics with relatively lower strain input compared to other MA methods, on the other hand it has the capability to produce nanocrystalline Cu-Fe multilayer structure, which has interesting magnetic behaviors [105-108].

The 25 μm thick Cu and Fe raw foils with a purity of 99.8% were cut and weighted out separately to achieve an average composition Cu40/Fe60 in atomic percent. Then the Cu and Fe foils were stacked as a Cu/Fe/Cu/Fe structure with different initial areal size. The cold rolling experiment was performed with a hand rolling mill with rollers. The time to accomplish a roll is approximately estimated as 1s and the multilayer foil was folded after a roll. The deformation level was described by the number of passes which consists of a roll and a fold. The phase transformation and structural evolution was measured by Bruker X-ray diffractometer (XRD). The microstructure was measured by FEI Titan scanning transmission electron microscope (STEM) with a CEOS probe aberration corrector and the composition was calculated from the electron energy loss spectrum (EELS) using the software Digital Micrograph. The STEM sample was prepared by Zeiss 1540XB cross beam focused ion beam (FIB) system with 30kv milling followed by a 5kv cleaning to minimize the surface contamination.

The Cu-Fe multilayer sample with nominal composition $Cu_{40}Fe_{60}$ was cold rolled up to 105 passes. Fig. 27(a) shows the XRD patterns of samples with small deformation input (after 15 passes) and larger deformation input (105 passes). After initial 15 rolling and folding passes, only individual sharp peaks corresponding to pure Cu and Fe can be observed. At this deformation level, no significant peak broadening and convolution is observed, which indicates good bonding has been achieved without intermixing and transformation reactions. As the deformation level increases to 105 rolling passes, the intensity of peaks decreases and a significant peak broadening, which is reflected by the increase of full width at half maximum (FWHM) of the peaks [Fig. 27(b)], can be observed. Sherrer's formula [109] was applied to estimate grain sizes and it was found that the grain sizes of Cu and Fe were significantly refined to about 14 nm after 105 rolling passes [Fig. 27(c)]. At 105 passes, the Cu peak and Fe peak convolute with each other making the valley of the XRD curve rise above the baseline. This indicates the intermixing occurred and the solid solution phase transformation was induced by the deformation. Since the emphasis of this work is to study the intermixing during the reaction while solid solution phase coexists with Cu and Fe, no more deformation input was applied and the microstructure and the composition profile across the multilayers were investigated on sample after 105 passes.

The STEM high angle annular dark field (HAADF) image of Cu-Fe multilayer sample after 105 rolling passes is seen in Fig. 28. Since the contrast of HAADF image is highly sensitive to atomic numbers (Z-contrast image), the bright layer corresponds to larger atomic number element, which is Cu, and dark layer corresponds to smaller atomic number element, which is Fe. It is noted that the layer thickness is not uniform but has a variation. This is resulted from the non-uniform strain distribution from the cold rolling that some areas are more deformed and some areas are less deformed. The layer thickness for both Cu and Fe observed from STEM

image is below 20 nm, which is consistent to XRD estimation. From the high resolution image [Fig. 28(b)] it is found that the grains are largely elongated. The columnar shapes result from the deformation and the layers tend to be parallel to the rolling direction. EELS measurement was performed across the multilayers and the drift-correction spectrum image was taken in the region of interest (ROI) [Fig. 29(a)]. The composition profile from A to B in Fig. 29(a) was obtained by analyzing the spectrum image since every point in the ROI has the spectrum information and it is shown in Fig. 29(b). Pure Cu (position K in Fig. 29(b)) and Fe regions (position B, D and F) are observed in the composition profile, which is consistent to the XRD observations. An Fe-rich solid solution with limited Cu solute is also observed (position H and J). Composition profiles of other areas across the multilayers were also measured and they show identical features as Fig. 29(b). Moreover, significant intermixing was observed in the profile as a Cu-rich solid solution (E and I) and a Fe-rich solid solution (A, C and G), which is consistent with the convolution of XRD peaks.

The composition profile between the pure phase and solid solution phase varies continuously and smoothly. This indicates Cu mixes into Fe and Fe mixes into Cu upon cold rolling and a solid solution phase with continuous composition variation was induced between pure components. Interestingly, in the profiles of all surveyed areas, a significant Cu local consumption is observed in regions that originally were pure Cu. However, little Fe local consumption was observed. One of the examples is illustrated in the F-G-H range in the profile. Initially before deformation, pure Cu was located between position F and H. After deformation more than 50 at. % Fe mixed into Cu to achieve a Fe-rich solid solution as shown at position G. However, Fe was not much affected by Cu mixing. Only about 6% Cu atomic percent (position H) was observed. This indicates Fe tends to mix into Cu preferentially than Cu mixing into Fe since the initial thickness is the same for both Cu and Fe. The difference in the compositions of the solid solution as well as degree of intermixing (positions A, C, E, G and I) can be attributed to the non-uniform strain distribution due to deformation. This results in certain local areas which undergo larger deformation and have a larger degree of intermixing thus a smaller Cu composition. The mixing asymmetry that Fe mixes into Cu preferentially than Cu mixing into Fe can be rationalized by the vacancy concentration. The melting point of Cu is about 450K lower than Fe indicating there are more vacancies in Cu than Fe. Even though Fe has BCC structure which has lower packing density and more open space than FCC Cu, the larger amount of vacancies in Cu enable a higher mobility of Fe in Cu than Cu in Fe. This behavior is similar as in thermally activated diffusion. The diffusion of Cu in Fe and Fe in Cu in the thermally activation are reported as in Eq. 14 [110] and 15 [111]. From Eq. 14 and 15, at low temperature (T < 1400K), $D_{Fe\ in\ Cu}$ is larger than $D_{Cu\ in\ Fe}$ at the same temperature.

$$D_{Cu\ in\ Fe} = 300\exp(-283.404/RT)\quad cm^2/s \tag{14}$$

$$D_{Fe\ in\ Cu} = 1.4\exp(-216.524/RT)\quad cm^2/s \tag{15}$$

Eq. 15 was applied to estimate the interdiffusion coefficient due to thermal activation at room temperature since Fe diffuses in Cu has a major contribution to the interdiffusion. The interdiffusion coefficient was estimated as 2.8×10^{-38} cm^2/s at T=300K. If the intermixing due to

cold rolling is regarded as a result of interdiffusion, the relationship between diffusion distance L and diffusion time t as in $L = 2\sqrt{Dt}$ was applied to estimate the effective interdiffusion coefficient. The effective interdiffusion coefficient due to cold rolling is estimated as 5.4×10^{-16} cm^2/s. This indicates the interdiffusion coefficient was promoted by 22 orders of magnitude compared to room temperature diffusion. The effective temperature concept [34], in which the diffusion coefficient under deformation at room temperature is equal to the effective diffusion coefficient under an effective temperature T_{eff} without deformation, can be applied to explain the promoted diffusion coefficient. If the promoted interdiffusion coefficient is attributed to such an effective temperature, T_{eff} can be estimated as 734K from Eq. 15. This effective temperature is not the physical temperature in the cold work since such a high temperature cannot be achieved because the rolling mill is massive compared to the sample. It is noted that though the effective temperature is estimated as 734K, the Cu and Fe are still immiscible at this temperature. This indicates that the intermixing was induced by deformation rather than any thermal effect. The columnar grain shape is also the effect of cold rolling rather than thermal effect in which the grain shape would be expected as equiaxed.

The kinetics of mechanical alloying and mixing behaviors are poorly understood. In this work, the composition profile across the multilayers of Cu-Fe immiscible system was revealed as a continuous variation between end members. Intriguingly, the diffusion profile of Cu/Nb multilayer, which is also an immiscible system with FCC/BCC structure, under high pressure torsion was revealed as an oscillation shape [112]. In our previous work, the profile of isomorphous Cu/Ni multilayer induced by cold rolling was found as an oscillation shape in the solid solution region [44] and the profile of cold rolled Ni/V multilayer shows a continuous variation. The results from all the investigations above indicate that the shape of composition profile between end members doesn't simply depend on one single factor such as solubility, crystal structures and enthalpy of mixing. It may depend on the interaction of these parameters as well as other parameters like atomic sizes and lattice parameters. How these parameters, if considered together, determine the kinetic pathways can be complicated and more effort needs to be done in order to have a better understanding in the mixing behavior in mechanical alloying.

In conclusion, the intermixing behavior of Cu/Fe multilayers induced by cold rolling was investigated. It was found that there is a continuous variation in the composition profiles across the multilayers between Cu and Fe. The mixing asymmetry was revealed that Fe mixes into Cu preferentially that Cu mixing into Fe, which is similar as in thermally activated diffusion. From comparisons of the present work and previous investigations, it can be seen that the mixing behavior is not simply determined by one single parameter but the correlation of different parameters.

Multilayer deformation of Ag-Pd

Conventionally, recrystallization process can be achieved by means of static recrystallization (SRX) or dynamic recrystallization (DRX). When thermal annealing is performed on pre-deformed crystalline materials, the dislocations generated as a result of deformation can be

eliminated by thermal annealing that leads to SRX [113]. DRX usually occurs when deformation is performed on crystalline materials at elevated temperature where dislocation accumulation due to deformation and elimination due to thermal effect occur simultaneously [114-116]. A well-established point of view is that although the storage energy induced by deformation plays as a driving force for recrystallization so that it is thermodynamically favored, thermal assistance is necessary to activate the recrystallization because dislocation motion is kinetically restricted at low temperature. Since recrystallization is considered as associated with dislocation movement[5], a challenging question is whether recrystallization can be induced without thermal assistance for some specific materials where dislocation movement occurs with ease. To answer this question, the recrystallization behaviors of Ag/Pd multilayers and monometallic Pd upon cold rolling were investigated in the present study. Ag/Pd multilayers were selected because the nanoscale microstructures mix with each other upon deformation, which makes the recrystallization process become more complicated and less understood since diffusion-induced grain boundary migration and diffusion induced recrystallization come into play [117]. Moreover, Ag and Pd has a complete solubility phase diagram [118] thus no intermetallic phase formation or amorphous formation can be induced, which helps to elucidate the mixing process and microstructural evolution. Monometallic Pd was selected because it has a face-centered cubic (FCC) crystal structure with high stacking fault energy [119]. High stacking fault energy allows for dislocation slip to occur with ease [115] and FCC structure enables cross-slip. By means of X-ray diffraction (XRD), scanning transmission electron microscope (STEM) and energy dispersive x-ray spectroscopy (EDX), it is observed that new grains were formed in the initial Ag60/Pd40 multilayer samples with consumption of pure Ag and Pd. The microstructure of new grains transformed from elongated to equiaxed shapes and a preferred composition of new grains that is close to the nominal sample composition was observed. Similar microstructural transformation was observed for Pd upon cold rolling as well.

For the Ag60/Pd40 multilayer samples, 25 μm thick Ag and Pd elemental foils with a purity of 99.8% were cut and weighed out separately to achieve an average composition Ag60/Pd40 in atomic percent. Then, the Ag and Pd foils were stacked as a Ag/Pd/Ag/Pd structure with different initial areal size. The cold rolling experiments were performed with a hand rolling mill. The time to accomplish a roll is approximately estimated as 1s and the multilayer foil was folded in half after each roll that reduced the sample thickness by 50%. For the monometallic Pd samples, the Pd foil with initial thickness 25 μm was used and it was rolled in the same way as described above. The deformation level was described by the number of passes in which one pass consisted of one fold and one roll. The phase transformation evolution was monitored with a Bruker D8 Advance X-ray diffractometer. The microstructure was examined with FEI Titan scanning transmission electron microscope that was equipped with an EDAX EDX detector. The TEM lamellas were prepared by Zeiss 1540XB cross beam focused ion beam (FIB) system with 30kv milling followed by a 5kv cleaning to minimize the surface contamination.

The XRD evolution for Ag/Pd multilayer samples after 25, 30, 35 and 40 passes is shown in Fig. 30. It is seen that after 25 passes, the convolution between individual peaks that correspond

to monometallic end members is above the baseline of the XRD pattern. This is clearly seen for Ag/Pd (111) and (200) diffraction peaks and it indicates that Ag and Pd have begun to mix with each other and form a solid solution phase. At 30 passes, an intermediate diffraction peak appears in between Ag and Pd diffraction peak which indicates the solid solution has become a distinct phase at this deformation stage. At 35 passes, the intermediate diffraction peak becomes the largest peak and the intensity of peaks corresponding to end members becomes relatively smaller. At 40 passes, the peaks corresponding to end members disappear and only the diffraction peak corresponding to the solid solution phase remains, which means the solid state reaction has reached a completion. In order to investigate the microstructural evolution of the multilayer samples, STEM experiments were performed and the results are shown in Fig. 31. From Fig. 31(a) and (b), it is seen that the grains were largely elongated as columnar shapes as a result of cold rolling for 25 and 30 passes and the layer thicknesses were refined to nanometer scale. Fig. 31(c) shows the microstructure of Ag/Pd multilayers after 35 passes where the thickness of solid solution layer expanded and equiaxed grains were observed in the solid solution region. One enlarged region in Fig. 31(d) clearly shows a grain that has an equiaxed shape. EDX was performed on an equiaxed grain as labeled A in Fig. 31(c) and both Ag and Pd signals were detected. This confirms that the equiaxed grains are newly formed solid solution grains and indicates that the microstructural change was accompanied with mixing induced by deformation.

XRD analysis was carried out in order to obtain the statistically averaged composition of new grains and the procedure is shown in Fig. 32. Fig. 32 (a) shows a XRD pattern of multilayers after 35 passes. It was then fitted with three peaks by applying Lorenz fitting program which is shown as the red curve in Fig. 32(a). The fitted curve was then deconvoluted into three individual peaks. The peak positions for Ag, Pd and solid solutions phases were obtained as the position of the deconvoluted peaks. This procedure was repeated for samples after 25, 30, 35 and 40 passes and the corresponding lattice parameters for each phase were calculated using Bragg's law [60]. The lattice parameters of Ag-Pd solid solution with different Pd composition are shown in Fig. 3(c) and data used in Fig. 3(c) is from Ref. 120. It can be seen that the lattice parameter variation of Ag-Pd system against Pd compositions satisfies Vegard's law [61] and it is fitted linearly shown as the red line in Fig. 32(c). By using the lattice parameters of solid solution phase obtained in Fig. 32(b) and relationship between lattice parameter and Pd composition [Fig. 32(c)], the Pd composition in the solid solution phase at each pass is calculated as shown in Fig. 32(d). It is seen that the solid solution phase induced by deformation has a preferred composition, which is about Pd 38 at. %, and it doesn't change significantly with further deformation.

An intriguing result is the intermediate diffraction peak in the XRD pattern, which indicates a distinct generation of grains was induced by cold rolling. This XRD result is in contrast to that from conventional volume diffusion due to thermal annealing, where the XRD evolution would have been predicted as that Ag peak continuously shifts towards Pd peak side and Pd peak doesn't shift but decreases in intensity [117]. This is because the diffusion coefficient of Pd diffusing into Ag is significantly larger than that of Ag diffusing into Pd at the same tempeture

[121], which causes Ag to be consumed sooner than Pd. However, no intermediate diffraction peak would have been predicted as result of volume diffusion. A statistically preferred composition of newly formed solid solution grains was observed to be the sample nominal composition. Since the mixing reaction has not completed for the multilayer samples after 30 and 35 passes, i.e. the solid solution coexists with Ag and Pd, the observation that the preferred composition of new grains is close to nominal composition is unexpected, since Ag and Pd have a complete mutual solubility.

Similarly, a preferred composition of Ag-Pd solid solution phase induced by annealing on Ag/Pd multilayer thin films has been observed by Baither et al [117]. They found that the preferred composition is about Pd 24.5 at. %. In the study of interdiffusion of Ni-Pd multilayer thin films subjected to annealing [122], it was demonstrated that several different preferred compositions of newly formed grains were established. The formation of new grains is rationalized as a result of diffusion-induced recrystallization and the preferred compositions are related to the ideal strength of materials [122]. However, the preferred composition of new grains due to cold rolling in this work is remarkably different from that induced by thermal annealing on multilayer thin films.

For monometallic Pd, the cross-section microstructures are shown in Fig 33. It is seen in Fig. 33(a) and (b) that the grains were elongated due to cold rolling for 20 passes. After additional 20 passes, the grains are in equiaxed shape as shown in Fig. 33(c). Since at each rolling process the sample was inserted between the rolling mills in a random direction, there is no significant distinction between longitudinal plane and transverse plane in the cross-section. This microstructural change clearly indicates that the recrystallization was induced by deformation.

The recrystallization observed in this work is considered as an athermal process and thermal assistance has been ruled out for following reasons. Firstly, significant temperature rise due to cold work is unlikely because the rolling mill is massive compared to the sample. Moreover, no significant heat was sensed during the manual operation in the rolling and folding process. In fact, even in the severe deformation as high pressure torsion (HPT), the temperature rise during deformation is not significant [73]. Secondly, recrystallization temperature is the temperature at which recrystallization is accomplished within one hour and it is generally considered as about $0.4\text{-}0.5T_m$ [115], where T_m is the melting point. If the recrystallization observed in this work is attributed to a thermal effect, the temperature rise caused by deformation has to be above 730K, since the T_m of Pd is 1825K [123]. It is noted that the time in which the sample was in contact with the rollers to accomplish each roll was approximately 1s. This means the recrystallization of monometallic Pd was accomplished within 40s, since all grains have transformed into equiaxed shapes after 40 passes [Fig. 33(c)]. Such a short time requires even significantly higher temperature than 730K to be achieved, which is implausible in the rolling process. Thirdly, the XRD patterns of $Ag_{60}Pd_{40}$ multilayers after deformation show significant distinction from what would be expected from thermal activation, which indicates thermal assistance didn't come into play. Fourthly, the effect of room temperature annealing is negligible since the STEM experiment was performed within a week after the as-rolled sample was achieved. Fifthly, STEM

sample preparation by FIB will cause temperature rise for no more than 10K for metals [124]. From all above aspects, it is evident that the recrystallization was induced athermally due to cold rolling rather than by any thermal assistance.

In conclusion, athermal recrystallization was induced during the cold rolling of Ag/Pd multilayers. The newly formed grains in the initial Ag/Pd multilayers due to deformation are in equiaxed shapes and have a statistically preferred composition that is close the nominal composition. This preferred composition is not expected from volume diffusion due to thermal activation and it is significantly different from what was induced by annealing on multilayer thin films. During the cold rolling of monometallic Pd, the elongated grains were induced by deformation and they transformed into equiaxed shapes upon further deformation. The results in this work show that for $Ag_{60}Pd_{40}$ multilayers and monometallic Pd, recrystallization can be achieved athermally at room temperature and thermal activation is not a necessary criterion.

References

[1]   Benjamin J, Volin T. Metall Trans 1974;5:1929.
[2]   Suryanarayana C. Prog Mater Sci 2001;46:1.
[3]   Koch C. Mater Sci Eng 1998;244:39.
[4]   Radlinski A, Calka A. Mater Sci Eng 1991;134:1376.
[5]   Koch CC, Whittenberger J. Intermetallics 1996;4:339.
[6]   Schwarz R, Petrich R, Saw C. J Non-Cryst Solids 1985;76:281.
[7]   Koch C, Cavin O, McKamey C, Scarbrough J. Appl Phys Lett 1983;43:1017.
[8]   Gente C, Oehring M, Bormann R. Phys Rev B 1993;48:13244.
[9]   Schultz L. Mater Sci Eng 1988;97:15.
[10]   Hellstern E, Schultz L. Appl Phys Lett 1986;48:124.
[11]   Sheng H, Ma E. Phys Rev B 2001;63:224205.
[12]   Sheng H, Ma E. J Metast Nanocryst Mater 2001;10:275.
[13]   Murty B, Ranganathan S. Int Mat Rev 1998;43:101.
[14]   Smith A, Bai C, Ade H, Spontak R, Balik C, Koch C. Macromol Rapid Commun 1998;19:557.
[15]   Srinivasarao B, Oh-Ishi K, Ohkubo T, Mukai T, Hono K. Scripta Mater 2008;58:759.
[16]   Styczynski A, Hartig C, Bohlen J, Letzig D. Scripta Mater 2004;50:943.
[17]   Sieber H, Park J, Weissmüller J, Perepezko J. Acta Mater 2001;49:1139.
[18]   Sagel A, Sieber H, Fecht H-J, Perepezko J. Acta Mater 1998;46:4233.
[19]   Ueji R, Tsuji N, Minamino Y, Koizumi Y. Acta Mater 2002;50:4177.
[20]   Huang J, Wu Y, Ye H. Appl Phys Lett 1995;66:308.
[21]   Huang J, Wu Y, Ye H. Acta Mater 1996;44:1201.
[22]   Kuhrt C, Schultz L. J Appl Phys 1993;73:1975.
[23]   Sasaki T, Yamamoto K, Honma T, Kamado S, Hono K. Scripta Mater 2008;59:1111.
[24]   Oh-Ishi K, Mendis C, Homma T, Kamado S, Ohkubo T, Hono K. Acta Mater 2009;57:5593.
[25]   Holt R, Aldridge S. J Nucl Mater 1985;135:246.
[26]   Iwahashi Y, Horita Z, Nemoto M, Langdon TG. Acta Mater 1998;46:3317.
[27]   Amouyal Y, Divinski S, Estrin Y, Rabkin E. Acta Mater 2007;55:5968.
[28]   Divinski SV, Ribbe J, Baither D, Schmitz G, Reglitz G, Rösner H, Sato K, Estrin Y, Wilde G. Acta Mater 2009;57:5706.
[29]   Zhilyaev A, Nurislamova G, Kim B-K, Baró M, Szpunar J, Langdon T. Acta Mater 2003;51:753.
[30]   Vorhauer A, Pippan R. Scripta Mater 2004;51:921.
[31]   Xu C, Horita Z, Langdon TG. Acta Mater 2007;55:203.
[32]   Ma E. Mater Trans 2006;47:1269.
[33]   Miettinen J. Calphad 2005;29:212.
[34]   Martin G, Bellon P. Solid State Phys 1996;50:189.
[35]   Enrique RA, Bellon P. Phys Rev Lett 2000;84:2885.
[36]   Lefakis H, Cain J, Ho P. Thin Solid Films 1983;101:207.
[37]   Balogh Z, Reda Chellali M, Greiwe G-H, Schmitz G, Erdélyi Z. Appl Phys Lett 2011;99:181902.
[38]   Roussel J-M, Bellon P. Phys Rev B 2006;73:085403.
[39]   Dutt M, Sen S, Barua A. Phys Status Solidi A 1979;56:149.

[40]   Helfmeier H, Feller‑Kniepmeier M. J Appl Phys 1970;41:3202.

[41]   Larson DJ, Prosa TJ, Ulfig RM, Geiser BP, Kelly TF. Local Electrode Atom Probe Tomography. New York:Springer; 2013.

[42]   Thompson K, Lawrence D, Larson D, Olson J, Kelly T, Gorman B. Ultramicroscopy 2007;107:131.

[43]   Nelson JB, Riley D. Proc Phys Soc 1945;57:160.

[44]   Wang Z, Perepezko J. Appl Phys Lett 2013;103:191904.

[45]   Drits V, Srodon J, Eberl D. Clays Clay Miner 1997;45:461.

[46]   Sauvage X, Dinda G, Wilde G. Scripta Mater 2007;56:181.

[47]   Sauvage X, Wetscher F, Pareige P., Acta Mater. 2005; 53:2127.

[48]   Ekiz EH, Lach TG, Averback RS, Mara NA, Beyerlein IJ, Pouryazdan M, Hahn H, Bellon P, Acta Mater. 2014; 72:178.

[49]   Cordero ZC, Schuh CA, Acta Mater. 2015; 82:123.

[50]   Liu C, Hartley P, Sturgess C, Rowe G, Int. J. Mech. Sci. 2005; 27:829.

[51]   Divinski S, Ribbe J, Schmitz G, Herzig C. Acta Mater 2007;55:3337.

[52]   Ilg P, Barrat J-L. Europhys Lett 2007;79:26001.

[53]   Ono IK, O'Hern CS, Durian D, Langer SA, Liu AJ, Nagel SR. Phys Rev Lett 2002;89:095703.

[54]   Lund AC, Schuh CA. Phys Rev Lett 2003;91:235505.

[55]   Wang Z, Perepezko J, Acta Mater. 2015; 87:68.

[56]   Wang Z, Perepezko J, Larson D, Reinhard D, J. Alloys Comp. (2014),
         http://dx.doi.org/10.1016/j.jallcom.2014.11.106 (in press).

[57]   McGill R, Tukey JW, Larsen WA, Am. Stat.1978; 32:12.

[58]   Baskes M, Angelo J, Bisson C. Modell Simul Mater Sci Eng 1994;2:505.

[59]   Adams JB, Foiles SM. Phys Rev B 1990;41:3316.

[60]   Bragg WL. Proc Cambridge Philos Soc vol. 17, 1913. p.4.

[61]   Denton AR, Ashcroft NW. Phys Rev A 1991;43:3161.

[62]   Matano C. Jpn. J. Phys 1933;8:109.

[63]   Hall LD. J Chem Phys 1953;21:87.

[64]   Crank J. The Mathematics of Diffusion. UK : Oxford University Press; 1979.

[65]   Davin A, Leroy V. Rev Metall 1963;60:275.

[66]   Straumal BB, Mazilkin AA, Baretzky B, Schuetz G, Rabkin E, Valiev RZ. Mater Trans 2012;53:63.

[67]   Million B, Růžičková J, Vřešťál J, Patoka V, Silantjev V, Kolesnik V. Czech. J Phys B 1980;30:541.

[68]   Dinsdale AT. Calphad 1991;15:317.

[69]   Watson A, Hayes F. J Alloys Compd 2001;320:199.

[70]   Ohtake M, Nonaka Y, Futamoto M. IEEE Trans Magn 2012;48:1589.

[71]   Heinrich B, Arrott A, Cochran J, Liu C, Myrtle K. J Vac Sci Technol A 1986;4:1376.

[72]   Wang Z, Li Y, Jona F, Marcus P. Solid State Commun 1987;61:623.

[73]   Oh-ishi K, Edalati K, Kim HS, Hono K, Horita Z. Acta Mater. 2013;61:3482.

[74]   Ashkenazy Y, Vo NQ, Schwen D, Averback RS, Bellon P. Acta Mater. 2012;60:984.

[75]   Vo NQ, Zhou J, Ashkenazy Y, Schwen D, Averback RS, Bellon P. JOM 2013;65:382.

[76]   Pouryazdan M, Schwen D, Wang D, Scherer T, Hahn H, Averback R, Bellon P. Phys.Rev. B 2012;86:144302.

[77]   Bellon P, Averback RS. Phys. Rev. Lett. 1995;74:1819.

[78]   Takeuchi A, Inoue A. Mater. Trans. 2005;46:2817.
[79]   Oehring M, Klassen T, Bormann R. J. Mat. Res. 1993;8:2819.
[80]   Fogagnolo J, Amador D, Ruiz-Navas E, Torralba J. Mat. Sci. Eng. A 2006;433:45.
[81]   Mukhopadhyay D, Suryanarayana C, Froes FS. Metall. Mater. Trans. A 1995;26:1939.
[82]   Kuhrt C, Schultz L. J. App. Phys. 1992;71:1896.
[83]   Birsan M, Fultz B, Anthony L. Phys. Rev. B 1997;55:11502.
[84]   Straumal B, Baretzky B, Mazilkin A, Phillipp F, Kogtenkova O, Volkov M, Valiev R. Acta Mater. 2004;52:4469.
[85]   Uenishi K, Kobayashi K, Ishihara K, Shingu P. Mat. Sci. Eng. A 1991;134:1342.
[86]   Xu J, Herr U, Klassen T, Averback R. J. Appl. Phys. 1996;79:3935.
[87]   Schilling P, Palshin V, Tittsworth R, He J, Ma E. Phys. Rev. B 2003;68:224204.
[88]   Sauvage X, Dinda G, Wilde G. Scr. Mater. 2007;56:181.
[89]   Sauvage X, Wetscher F, Pareige P. Acta Mater. 2005;53:2127.
[90]   Hickenboth CR, Moore JS, White SR, Sottos NR, Baudry J, Wilson SR. Nature 2007;446:423.
[91]   Wu D, Lenhardt JM, Black AL, Akhremitchev BB, Craig SL. J Amer Chem Soc 2010;132:15936.
[92]   Piermattei A, Karthikeyan S, Sijbesma RP. Nature Chem 2009;1:133.
[93]   Foreman A. Acta Metall 1955;3:322.
[94]   Zhilyaev AP, Gubicza J, Suriñach S, Baró MD, Langdon TG. Mater Sci Forum vol. 426: Trans Tech Publ, 2003. p.4507.
[95]   Ma E, Atzmon M, Pinkerton F. Journal of applied physics 1993;74:955.
[96]   Xu J, Collins G, Peng L, Atzmon M. Acta materialia 1999;47:1241.
[97]   Qi M, Zhu M, Yang D, J Mater Sci Lett 1994;13:966.
[98]   Huang J, He A, Wu Y, Nanostruct Mater 1994;4:1.
[99]   He L, Ma E. Nanostruct Mater 1996;7:327.
[100] Gaffet E, Harmelin M, Faudot F. J Alloys Compd 1993;194:23.
[101] Huang J, Jiang J, Yasuda H, Mori H. Phys Rev B 1998;58:R11817.
[102]   Eckert J, Holzer J, Krill iII C, Johnson W. J Appl Phys 1993;73:2794.
[103]   Schilling P, Palshin V, Tittsworth R, He J, Ma E. Phys Rev B 2003;68:224204.
[104]   Schilling P, He J, Tittsworth R. Acta Mater 1999;47:2525.
[105]   Bakkaloğlu Ö. J Magn Magn Mater 1998;182:324.
[106]   Jin Q, Xu Y, Zhai H, Hu C, Lu M, Bie Q, Zhai Y, Dunifer G, Naik R, Ahmad M. Phys Rev Lett 1994;72:768.
[107]   Piraux L, Fert A, Schroeder P, Loloee R, Etienne P. J Magn Magn Mater 1992;110:L247.
[108] Pizzini S, Baudelet F, Chandesris D, Fontaine A, Magnan H, George J, Petroff F, Barthelemy A, Fert A, Loloee R. Phys Rev B 1992;46:1253.
[109]   Cullity BD, Stock SR. Elements of X-Ray Diffraction, third ed. New Jersey : Prentice-Hall Inc; 2001.
[110]   Yavari A, Desre P, Benameur T. Phys Rev Lett 1992;68:2235.
[111]   Salje G, Feller-Kniepmeier M. J Appl Phys 1977;48:1833.
[112]   Mackliet CA. Physical Review 1958;109:1964.
[113]   Cram D, Zurob H, Brechet Y, Hutchinson C. Acta Mater 2009;57:5218.
[114]   Luton M, Sellars C. Acta Metall 1969;17:1033.
[115]   Sakai T, Jonas JJ. Acta Metall 1984;32:189.

[116]   Doherty R, Hughes D, Humphreys F, Jonas J, Jensen DJ, Kassner M, King W, McNelley T, McQueen H, Rollett A. Mater Sci Eng A 1997;238:219.

[117]   Baither D, Kim T, Schmitz G. Scr Mater 2008;58:99.

[118]   Morioka S, Hasebe M. J Phase Equilib 1999;20:244.

[119]   Edalati K, Horita Z, Acta Mater 2011; 59:6831.

[120]   Rao CN, Rao KK. Can J Phys 1964;42:1336.

[121]   Adams J, Foiles S, Wolfer W. J Mater Res 1989;4:102.

[122]   Kasprzak M, Baither D, Schmitz G. Acta Mater 2011;59:1734.

[123]   Jones TP and Hall KG, Metrologia 1979; 15:161.

[124] Giannuzzi LA, Stevie FA, *Introduction to focused ion beams: instrumentation*, theory, techniques and practice. (Springer, 2005) p. 311.

Appendix 1

The layer thickness distribution follows a log-normal distribution and two assumptions about the layer thickness analysis have been made in order to illustrate the transformation kinetics. The first assumption is that the fraction of reaction is the integration of lognormal distribution from 0 to a threshold value and this threshold value remains the same at different number of passes. Second is that the log-mean and log-variance change with number of passes follows $\mu(n) = a/n$ and $\sigma(n) = b/n$, in which n is the number of passes and a and b are the constants to be determined. Then, the fraction transformed can be written as in the following equation.

$$f = \int_0^{Threshold} \frac{1}{\sqrt{2\pi}\sigma(n) \cdot t} \exp(-\frac{(\ln t - \mu(n))^2}{2\sigma(n)^2})$$

After the integration, the fraction is expressed as

$$f = \frac{1}{2} + \frac{1}{2} erf(\frac{\ln t \big|_0^{Threshold} - \mu(n)}{\sqrt{2}\sigma(n)}) = \frac{1}{2} + \frac{1}{2} erf(\frac{C - \mu(n)}{\sqrt{2}\sigma(n)})$$

where C is an integration constant. When $\mu(n) = a/n$ and $\sigma(n) = b/n$, the fraction could be expressed as

$$f = \frac{1}{2} + \frac{1}{2} erf(\frac{Cn}{\sqrt{2b}} - \frac{a}{\sqrt{2b}})$$

where C, a, and b can be obtained from the experimental measurements. From the experimental measurements, at the 36 passes the fraction f is 0.4. The log-mean is 1.5 and the log-variance is 0.3. Thus

$$0.4 = \frac{1}{2} + \frac{1}{2} erf(\frac{C - \mu(n)}{\sqrt{2}\sigma(n)}) = \frac{1}{2} + \frac{1}{2} erf(\frac{C - 1.5}{\sqrt{2} \cdot 0.3})$$

From above the constant C is 1.4. Correspondingly

$$b = \frac{C}{\sqrt{2} \cdot 0.08} = 12.4$$

$$a = 3\sqrt{2}b = 52.6$$

The log-mean and log-variance both decrease when n increases. At the extreme condition when n is equal or larger than 60 where the reaction completes, the variance of layer thickness should be zero. Thus the variance should decrease when n increases at least in the large n value range.

In conclusion, the analysis has been conducted by the assumptions that the fraction of reaction is the integration of lognormal distribution from 0 to a threshold value, the log-mean follows the relationship $\mu(n) = 52.6/n$ and log-variance follows $\sigma(n) = 12.4/n$. It leads to the consistence to the expression of fraction and number of passes as

$$f = \frac{1}{2} + \frac{1}{2} erf(0.08n - 3)$$

from both the model and experiment. Since there is a negligible volume change upon mixing, the mixing layers per rolling pass can be expressed as

$$l_{mix} = 396697 * \frac{df}{dn} = 22443 * \exp(-(0.08n - 3)^2)$$

which is illustrated in Fig. 12.
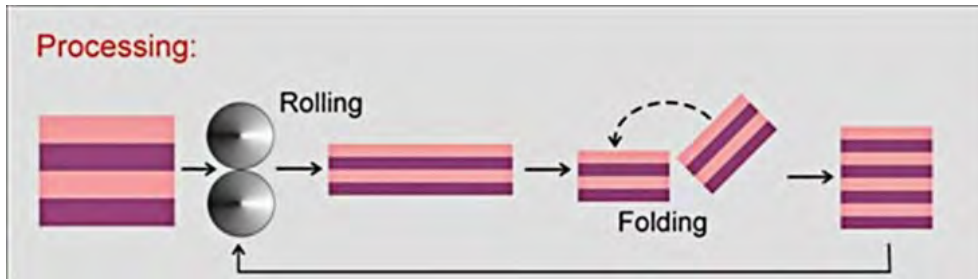
Fig. 1 Schematic illustration of the cold rolling process
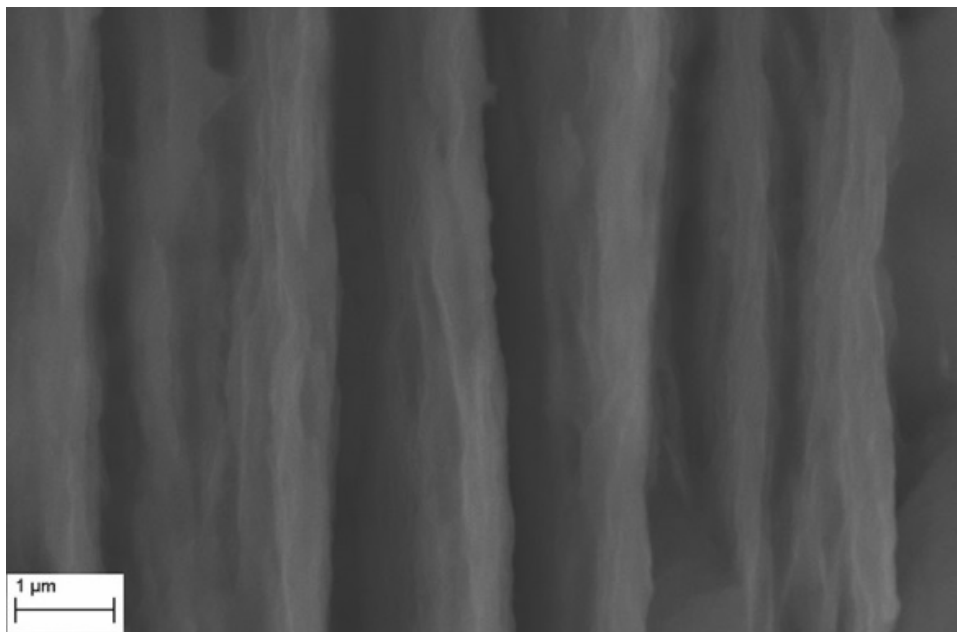
Fig. 2 Secondary electron SEM image with Inlens detector of $Cu_{60}Ni_{40}$ multilayer cross-section morphology after 35 passes.
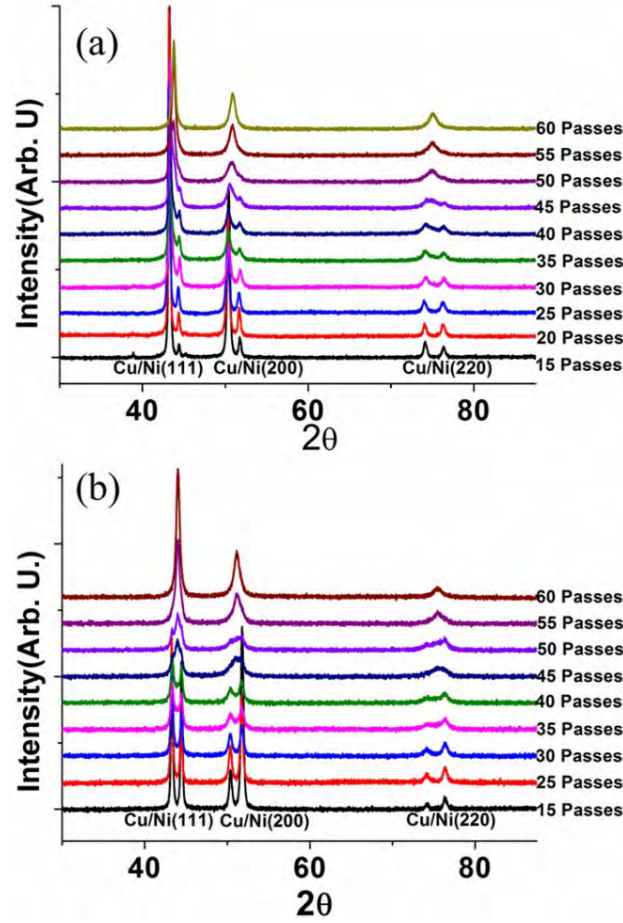
Fig. 3 X-ray diffraction between 10°-90° 2θ with increasing deformation for (a) $Cu_{60}Ni_{40}$ and (b) $Cu_{40}Ni_{60}$ multilayer samples. The peaks from left to right in each figure are Cu (111), Ni (111), Cu (200), Ni (200), Cu (220) and Ni (220) respectively.
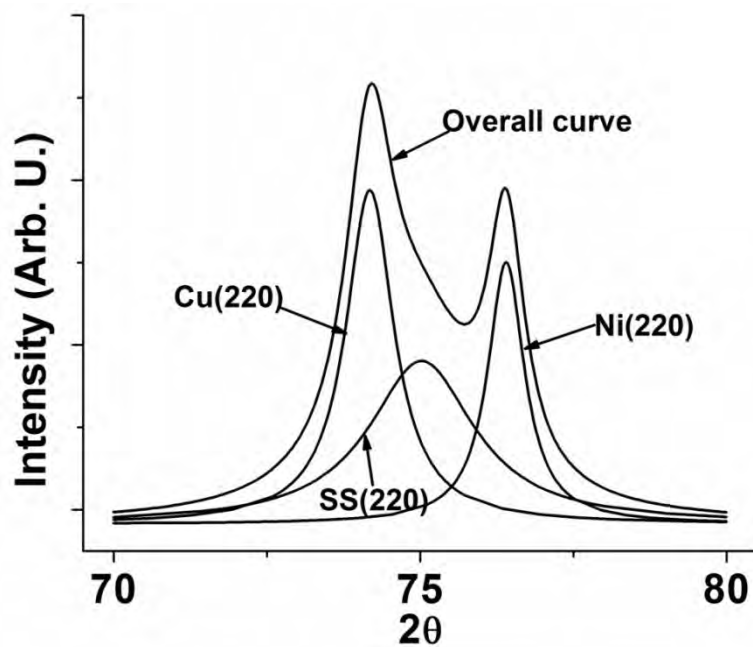
Fig. 4 The diffraction pattern and deconvolution method of $Cu_{60}Ni_{40}$ multilayer samples after 40 rolling passes. The peaks shown in the figure are overall diffraction pattern, Cu (220) deconvoluted peak, solid solution convolution peak (220) and Ni (220) deconvoluted peak as labeled respectively.
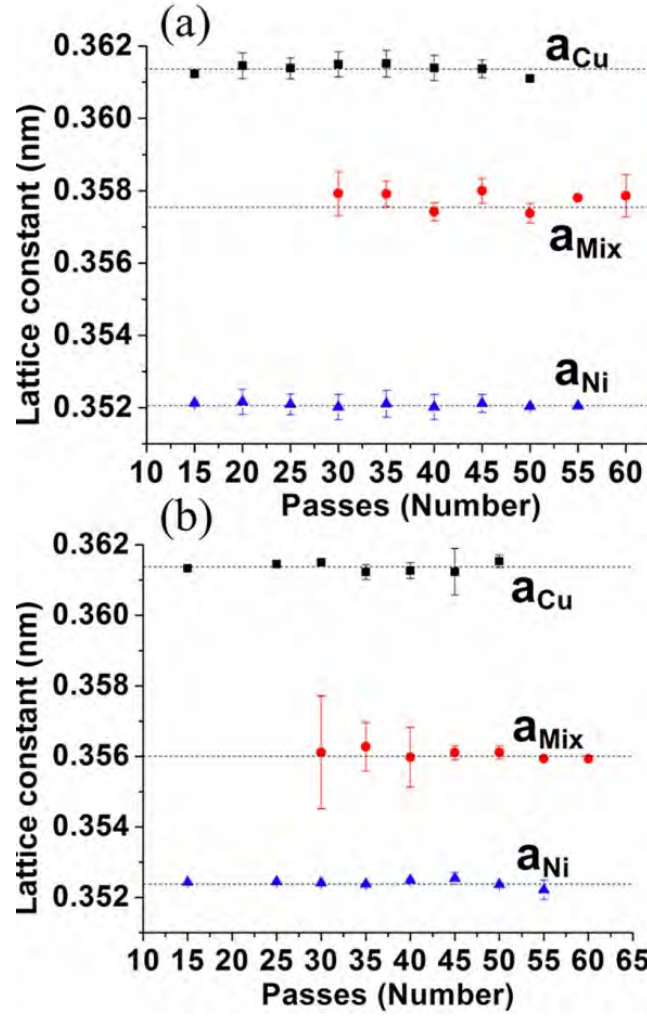
Fig. 5 The lattice constant behavior with increasing deformation for (a) $Cu_{60}Ni_{40}$ and (b) $Cu_{40}Ni_{60}$ multilayer. The reference lines from top to bottom in (a) are Cu, solid solution $Cu_{60}Ni_{40}$, and Ni respectively. The reference lines from top to bottom in (b) are Cu, solid solution $Cu_{40}Ni_{60}$, and Ni respectively.
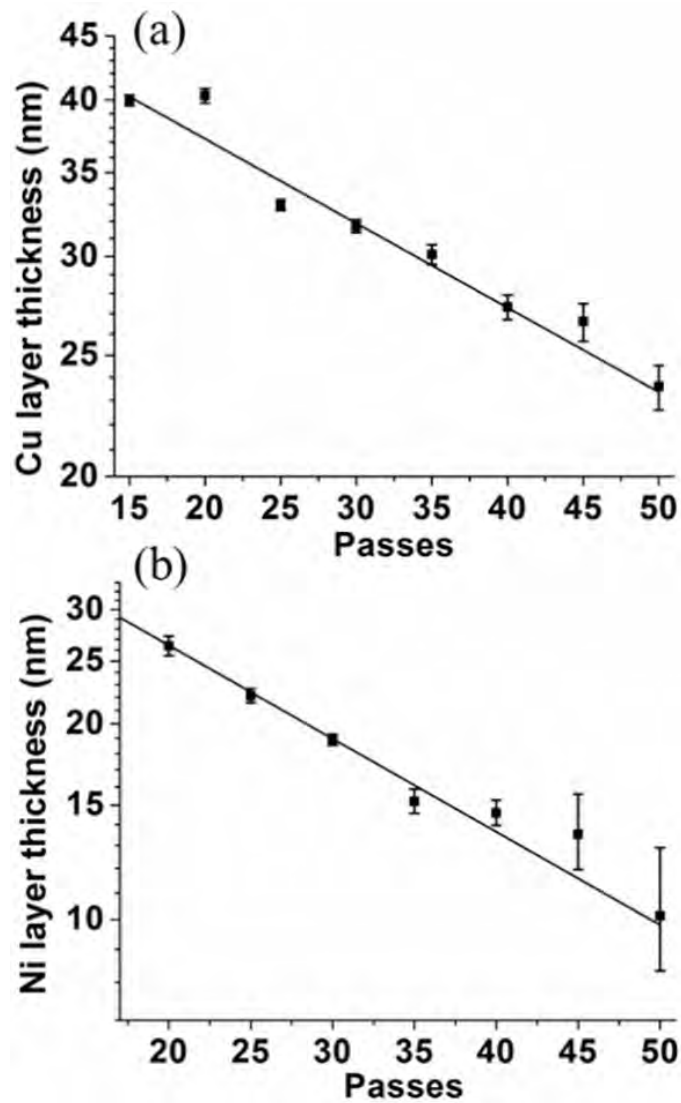
Fig. 6 (a) Cu (b) Ni layer thickness estimation by applying Sherrer's formula. The layer thickness is shown on a log scale and the number of passes is shown on a linear scale.
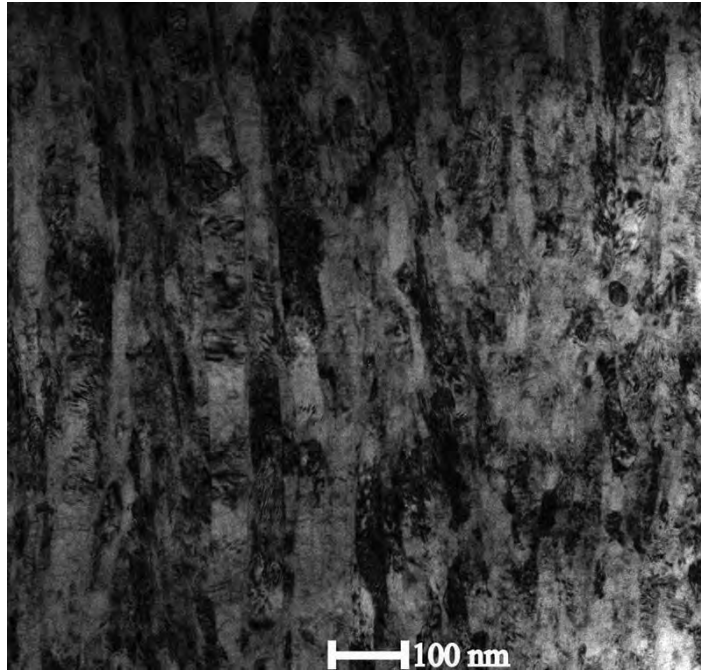
Fig. 7 Dark field TEM image showing the multilayer cross-section micro structure of the $Cu_{60}Ni_{40}$ as-rolled sample after 36 passes. The multilayers are in the vertical direction in the figure.
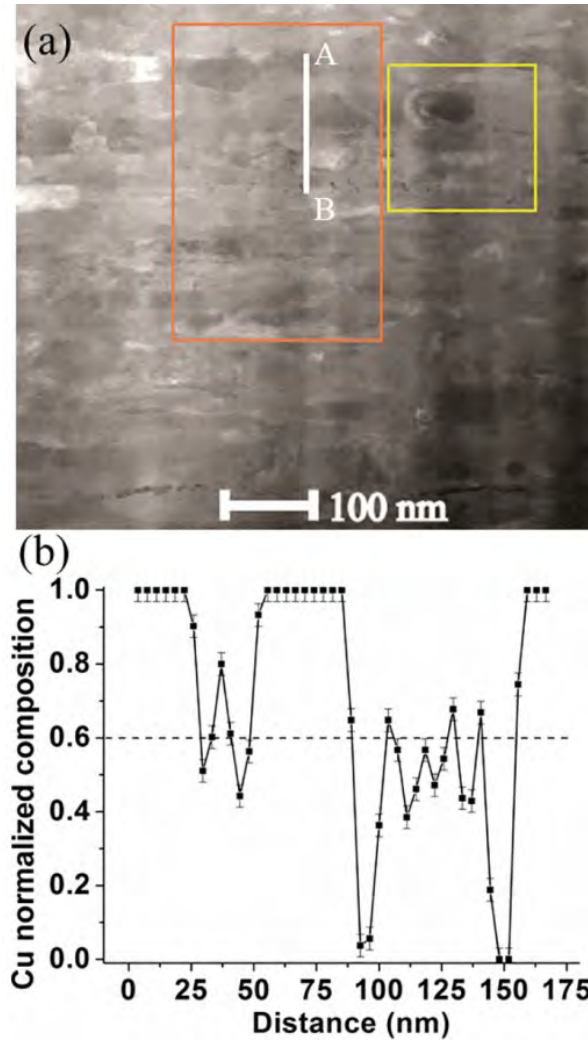
Fig. 8 STEM observation and analysis of as-rolled $Cu_{60}Ni_{40}$ multilayer after 36 passes. (a) STEM image showing the micro structure of the multilayer. The orange rectangle box is the region where EELS was taken. The yellow square box is the reference box for drift correction. (b) Normalized Cu composition in atomic fraction along the inset line in (a) from A to B. Horizontal line in (b) represents the overall multilayer composition.
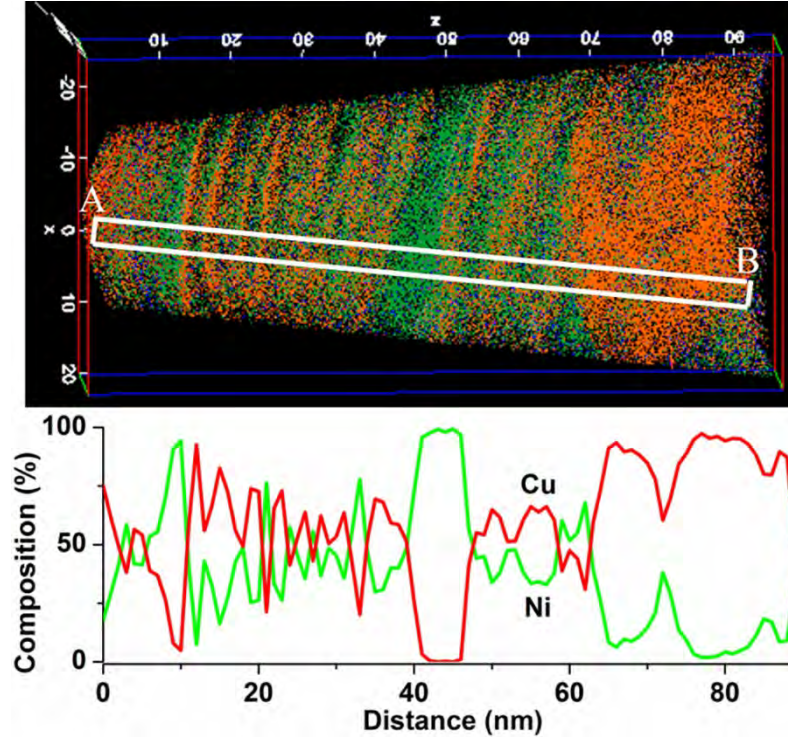
Fig. 9 Atom probe observation of $Cu_{60}Ni_{40}$ as-rolled sample after 36 passes. (a) Cross-section view of the 3-D reconstruction. The orange and green dots in (a) correspond to Cu and Ni respectively. (b) Composition profile along the white box inset in (a) from A to B.
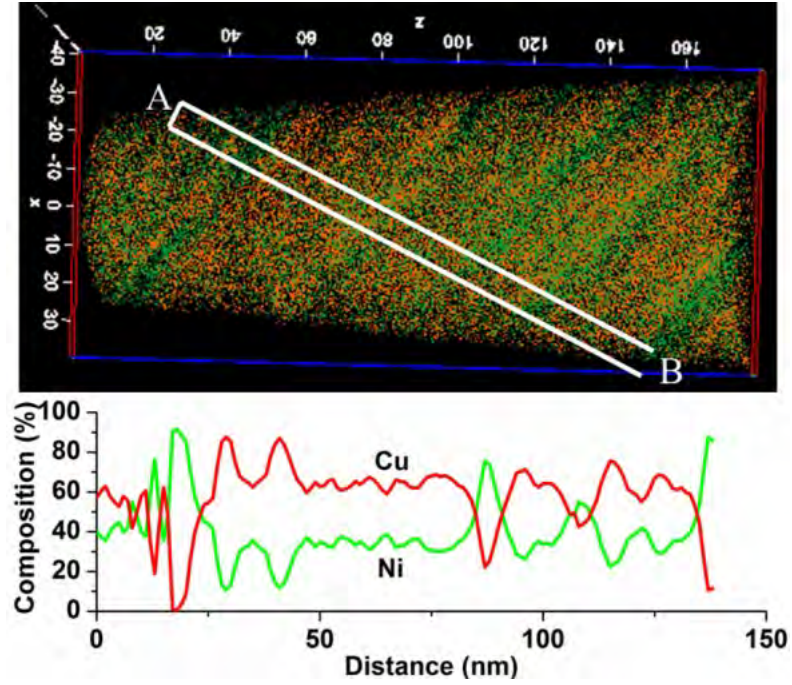
Fig. 10 Atom probe observation of $Cu_{60}Ni_{40}$ as-rolled sample after 46 passes. (a) Cross-section view of the 3-D reconstruction. The orange and green dots in (a) correspond to Cu and Ni respectively. (b) Composition profile along the white box inset in (a) from A to B.
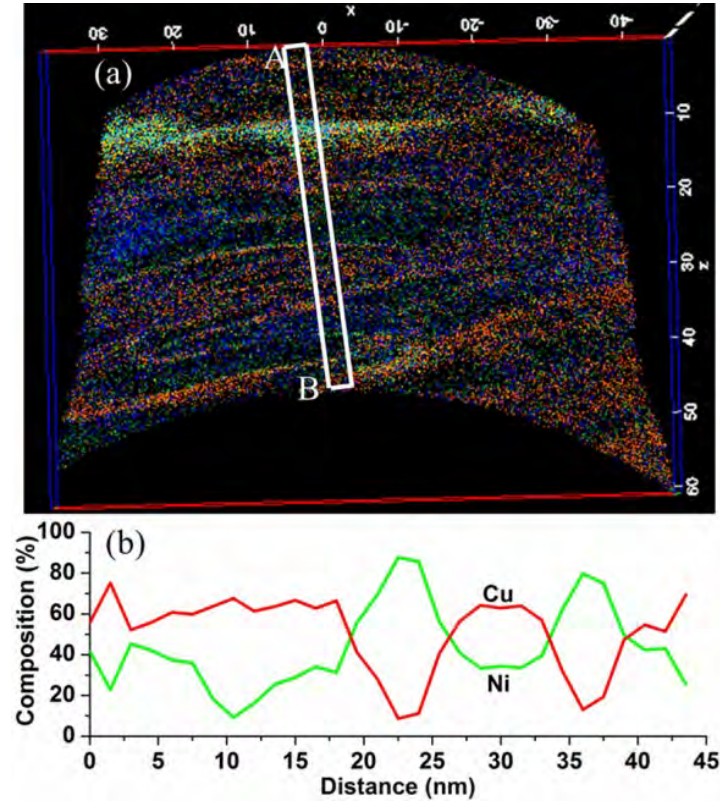
Fig. 11 Atom probe observation of $Cu_{60}Ni_{40}$ as-rolled sample after 60 passes. (a) Cross-section view of the 3-D reconstruction. The orange and green dots in (a) correspond to Cu and Ni respectively. (b) Composition profile along the white box inset in (a) from A to B.
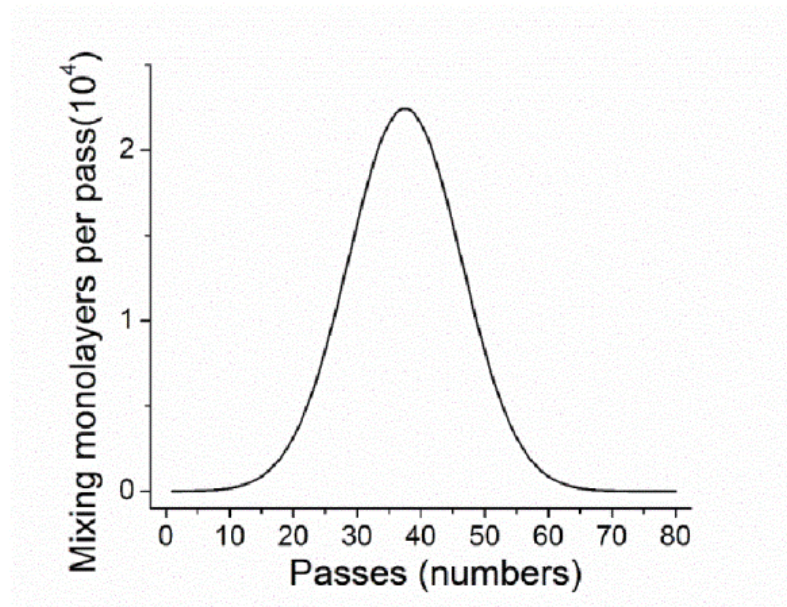
Fig. 12 The mixing layers yielding the solid solution phase per rolling pass according to the number of passes.
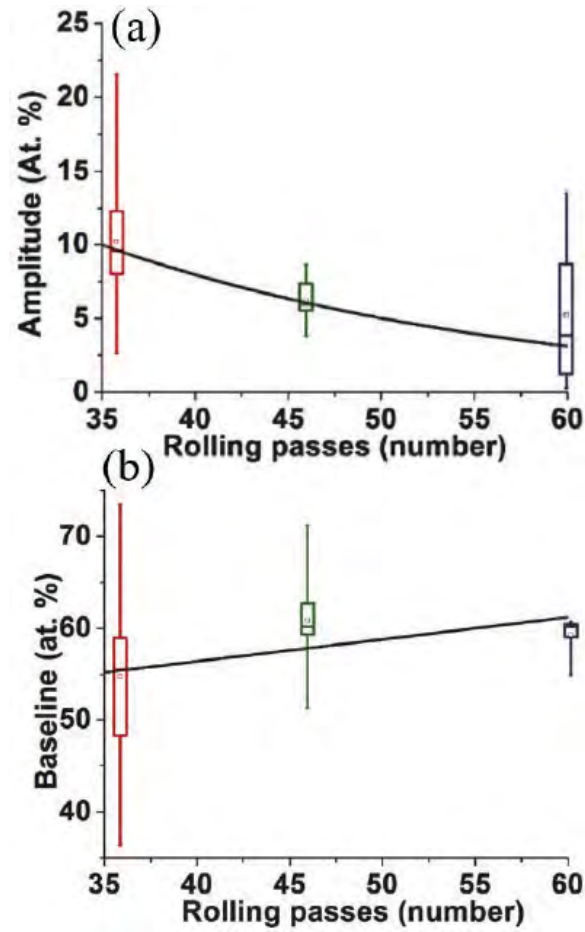
Fig. 13 (a) The box plots of the amplitudes at 36, 46 and 60 rolling passes. (b) The box plots of the baselines at 36, 46 and 60 rolling passes. In each box plot, the edges of the box stand for the 25% and 75% percentile, the whiskers stand for the maximum and minimum, the bar in the box stands for the median and the square in the box stands for the mean.
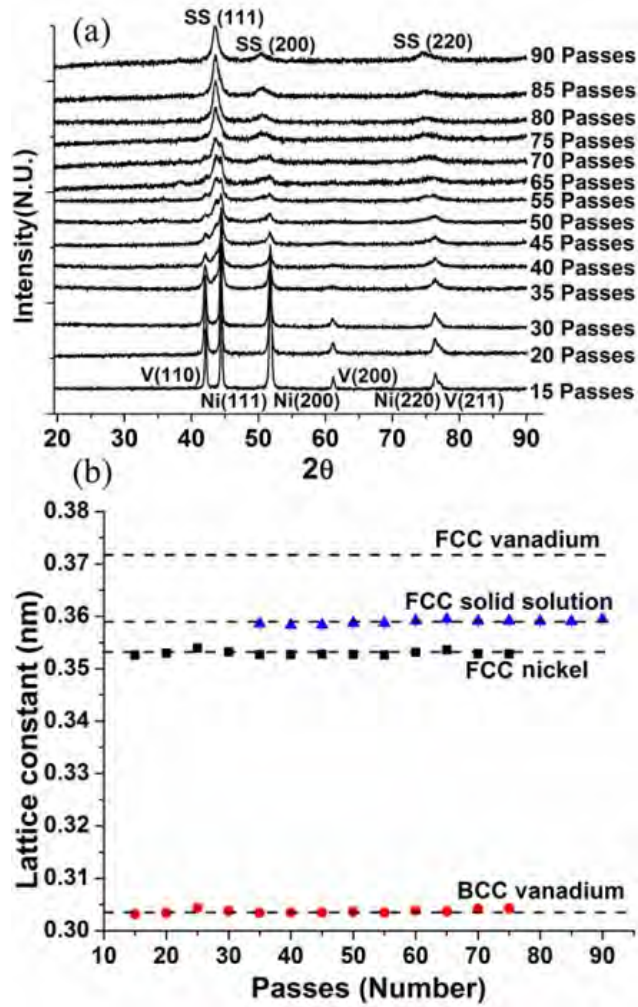
Fig. 14 (a) X-ray diffraction patterns for $Ni_{70}V_{30}$ multilayer. The pattern intensity was normalized for each pass. The corresponding diffraction peaks are labeled in the figures. The label SS stands for solid solution. (b)The lattice constants of Ni, V and solid solution phase with an average composition $Ni_{70}V_{30}$ at different rolling passes. The lattice constant of FCC vanadium is also labeled as a dashed line.
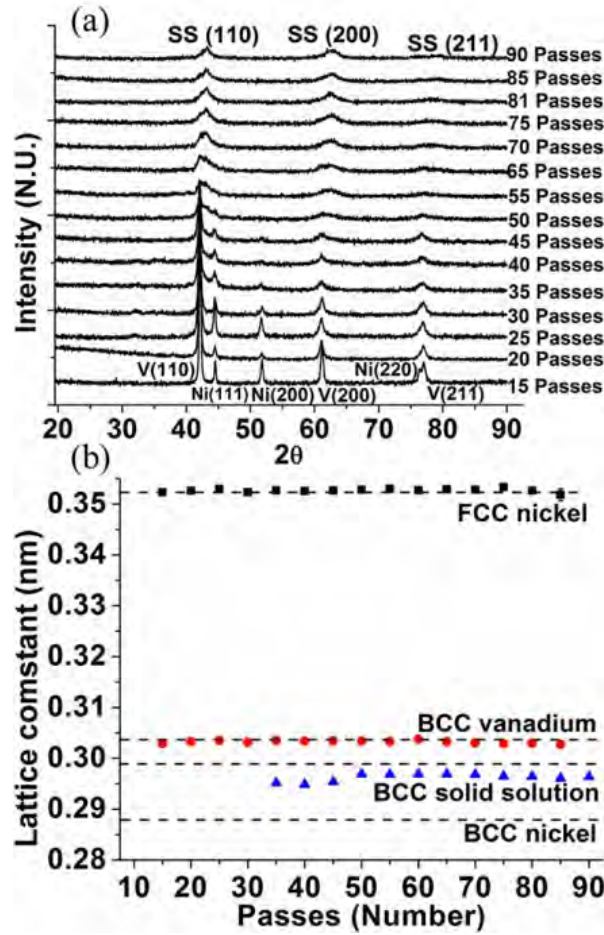
Fig. 15 (a)X-ray diffraction patterns for $Ni_{30}V_{70}$ multilayer. The pattern intensity was normalized for each pass. The corresponding diffraction peaks are labeled in the figures. The label SS stands for solid solution. (b) The lattice constants of Ni, V and solid solution phase with an average composition $Ni_{30}V_{70}$ at different rolling passes. The lattice constant of BCC nickel is also labeled as a dashed line.
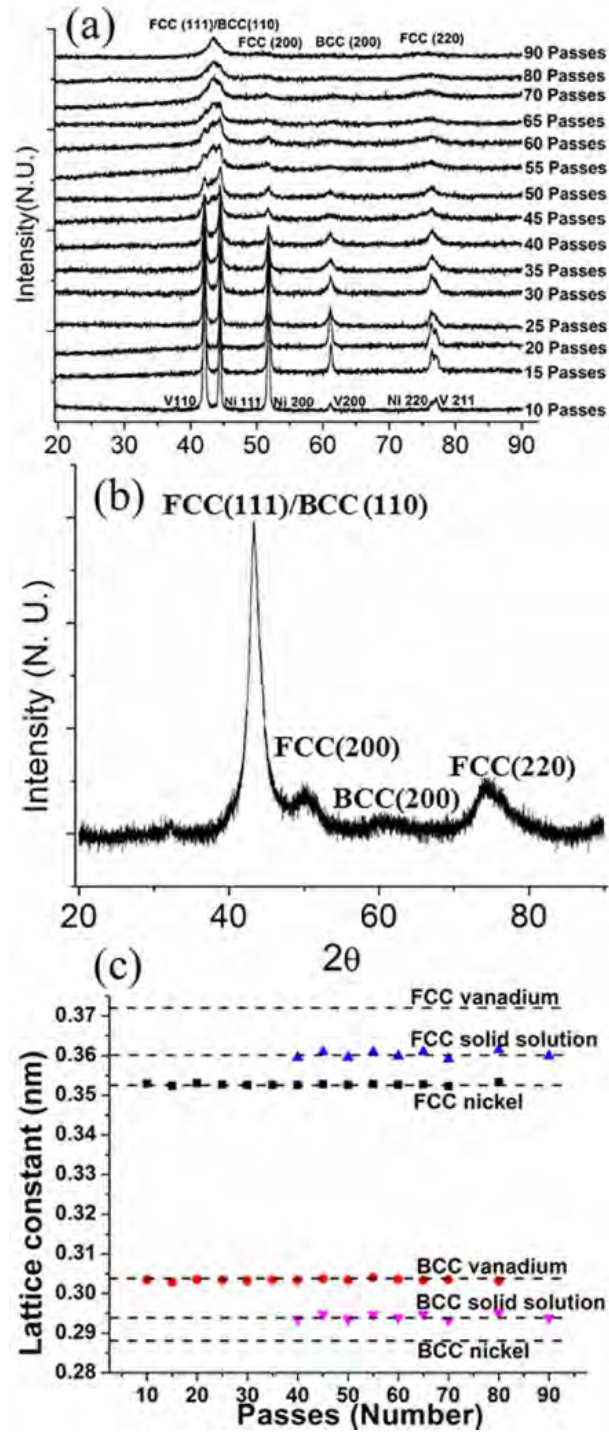
Fig. 16 (a) X-ray diffraction patterns for $Ni_{57}V_{43}$ multilayer. The pattern intensity was normalized for each pass. The corresponding diffraction peaks are labeled in the figures. The label FCC and BCC stand for FCC and BCC solid solutions respectively. (b) X-ray diffraction pattern for $Ni_{57}V_{43}$ multilayer after 100 rolling passes. The label FCC and BCC stand for FCC and BCC solid solutions respectively. (c) The lattice constants of Ni, V and solid solution phases with an average composition $Ni_{57}V_{43}$ at different rolling passes. The lattice constants of BCC nickel and FCC vanadium are also labeled as dashed lines.
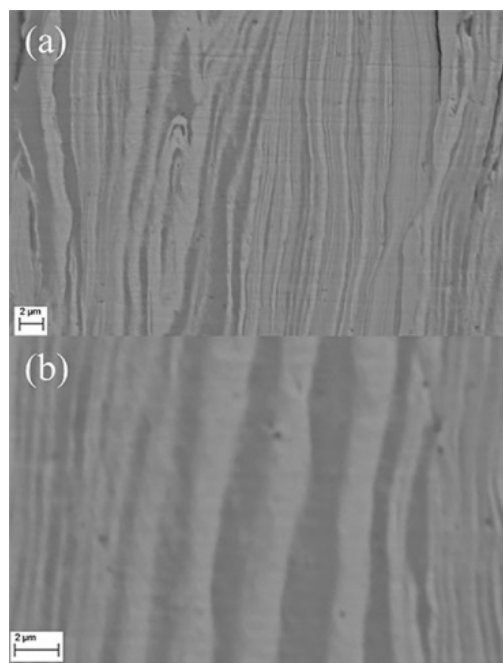
Fig. 17 (a) and (b) SEM images of $Ni_{51}V_{49}$ multilayer cross-sections after 30 rolling passes showing that the layers are in irregular shapes with non-uniform layer thickness.
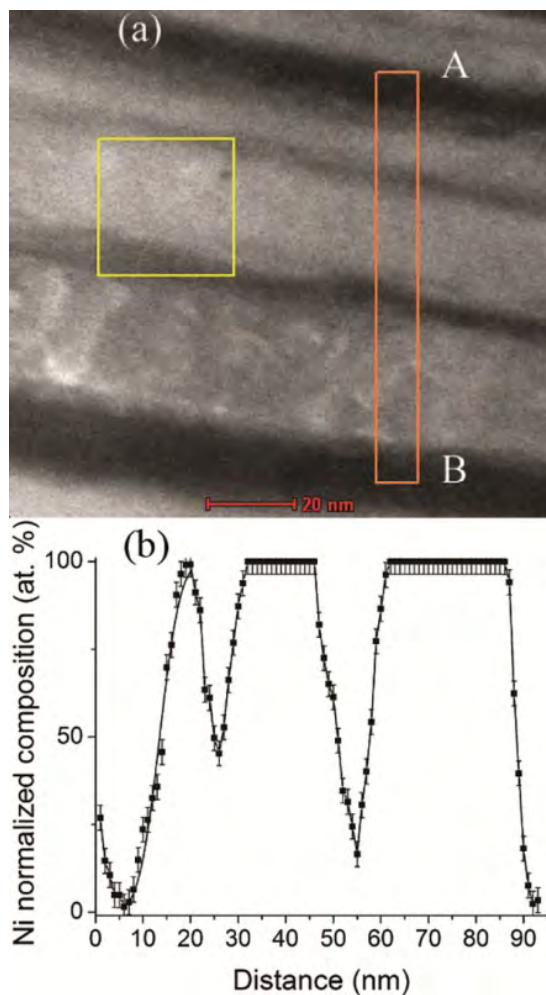
Fig. 18 (a) The STEM image of sample $Ni_{70}V_{30}$ after 60 passes showing the nanoscale multilayer structure. The yellow square box to the left is the reference box for drift correction. The orange rectangle box to the right is the area where EELS was taken. (b) The composition profile from A to B in (a) obtained from EELS quantification.
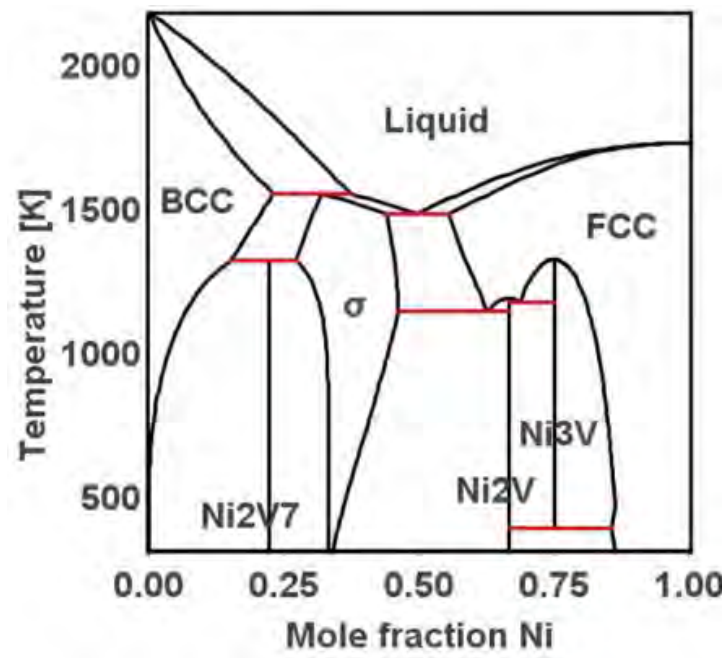
Fig. 19 Ni-V binary phase diagram obtained from Thermo-Calc software.
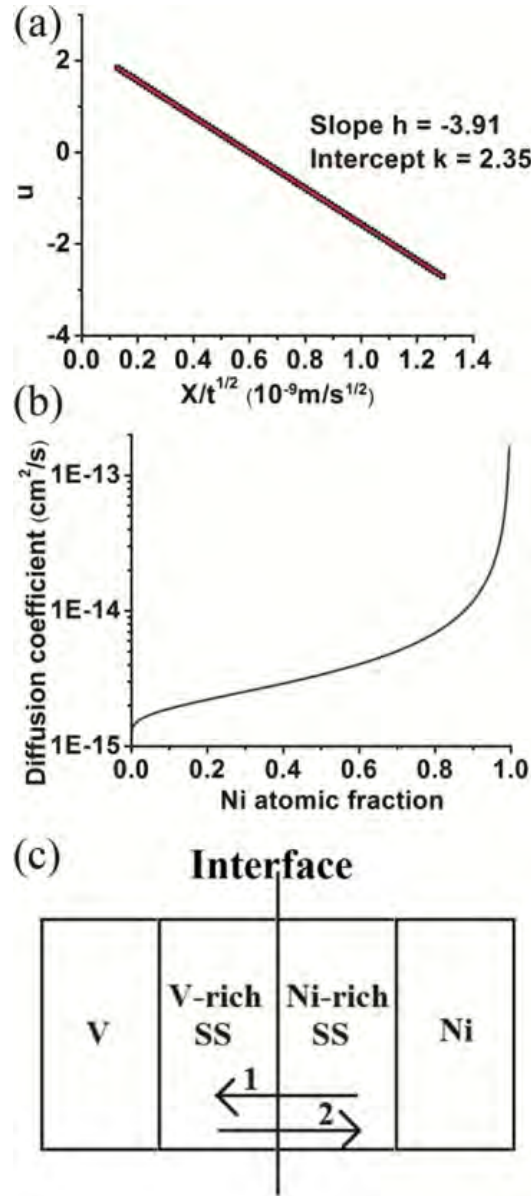
Fig. 20 (a) The probability plot of Ni composition fraction vs $X/t^{1/2}$. The slope and intercept are labeled in the figure. (b)The composition dependent diffusion coefficient derived from the analytical analysis. The diffusion coefficient at y-axis is expressed in logarithm. (c) Schematic illustration of interdiffusion process. Arrow 1 is the Ni diffusion direction and arrow 2 is the V diffusion direction.
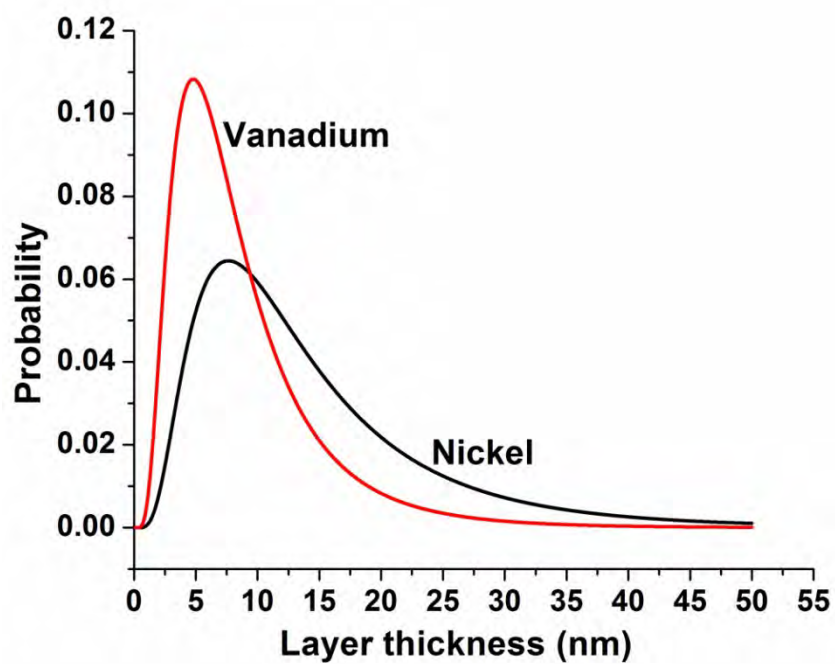
Fig. 21 Ni and V layer thickness distribution for $Ni_{70}V_{30}$ multilayer sample after 60 passes.
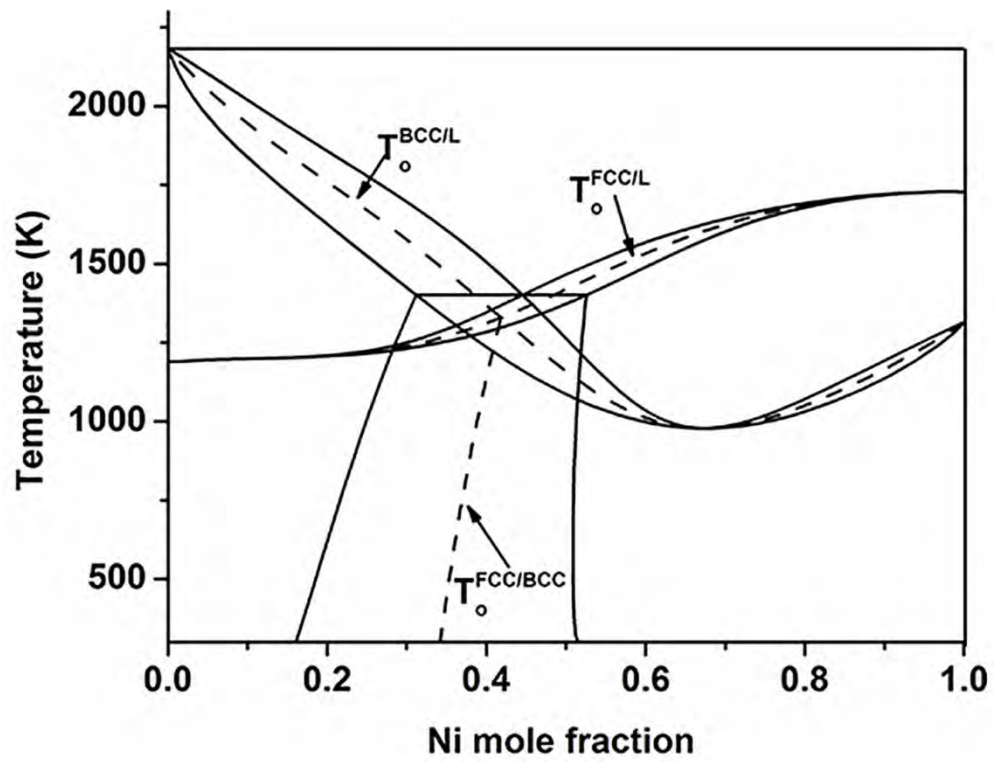
Fig. 22 To lines for BCC/liquid, FCC/liquid and FCC/BCC in Ni-V binary phase diagram. Only FCC, BCC and liquid phases without any intermetallic phase are shown in the phase diagram.
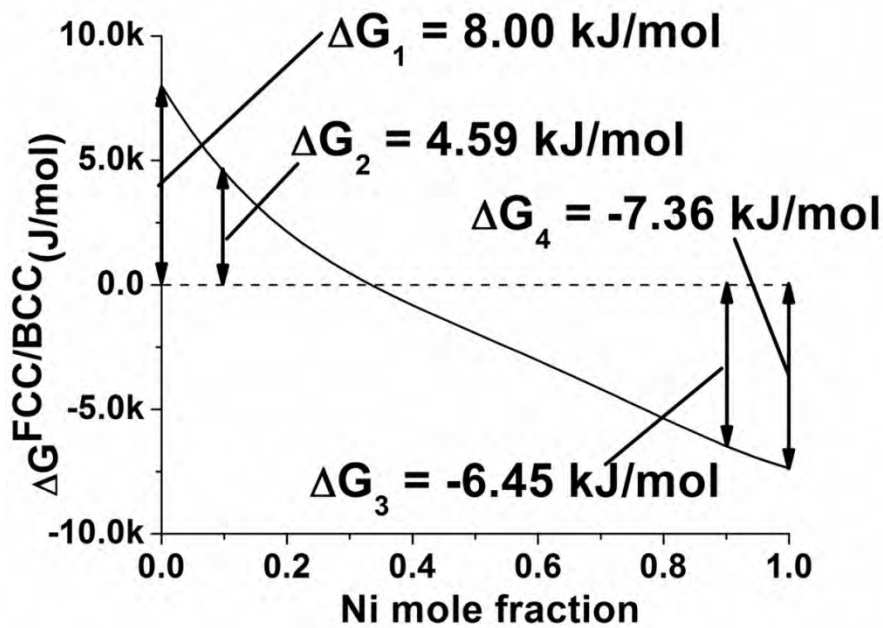
Fig. 23 The Gibbs energy difference between FCC and BCC phases. The Gibbs energy required to transform BCC V to FCC V is 8.00 kJ/mol and it is labeled as ΔG_1.The Gibbs energy required to transform BCC to FCC at 0.1 Ni mole fraction is 4.59 kJ/mol and it is labeled as ΔG_2. The Gibbs energy required to transform FCC to BCC at 0.9 Ni mole fraction is 6.45 kJ/mol and it is labeled as ΔG_3. The Gibbs energy required to transform FCC Ni to BCC Ni 7.36 kJ/mol and it is labeled as ΔG_4.
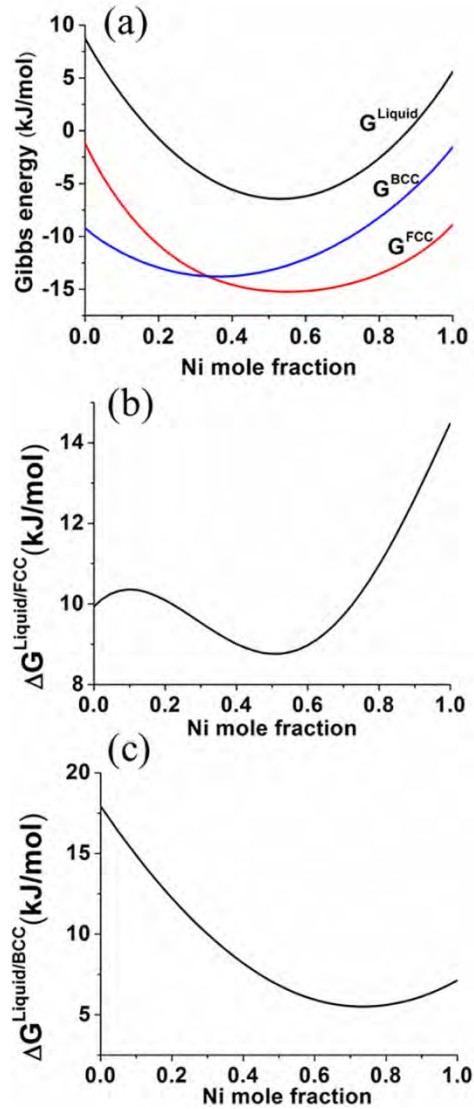
Fig. 24(a) The Gibbs energies of liquid (black curve), FCC (red curve) and BCC (blue curve) phases at room temperature. (b) The Gibbs energy difference between liquid and FCC phases. (c) The Gibbs energy difference between liquid and BCC phases.
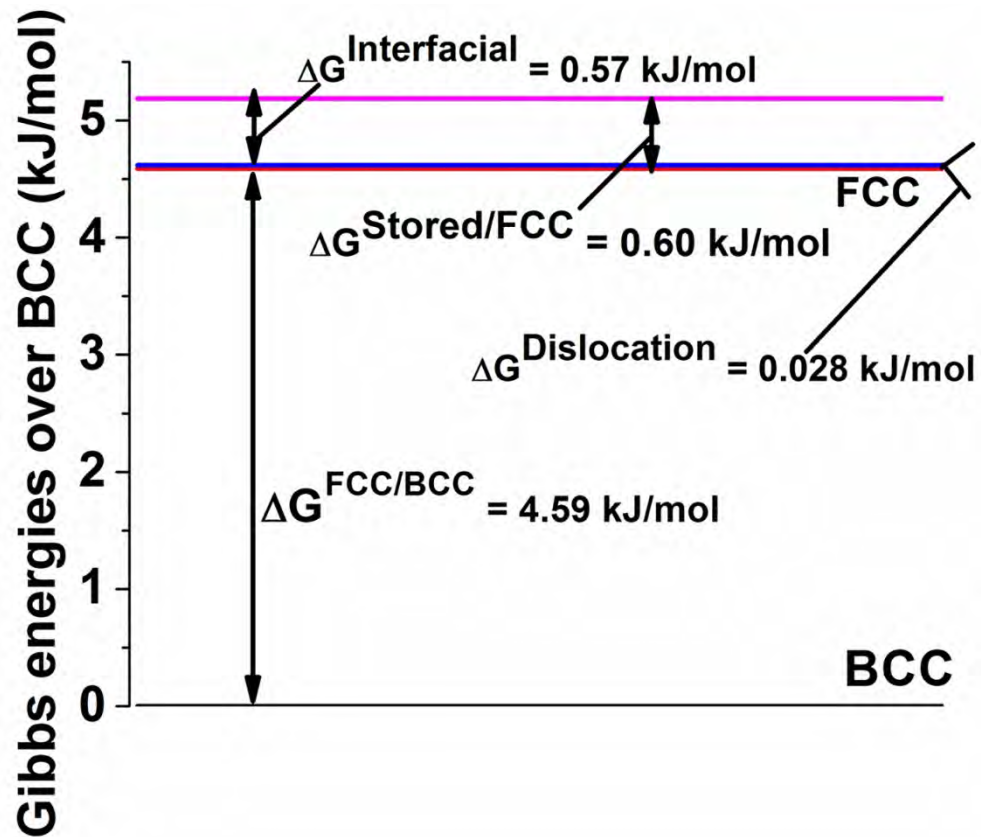
Fig. 25 The Gibbs energies relative to BCC phase for Ni mole fraction 0.1, where Gibbs energy for BCC phase is regarded as a reference. The energy increases due to BCC-FCC transformation, dislocation and interfacial area are labeled. The total stored energy on FCC phase due to deformation is also labeled in the figure.
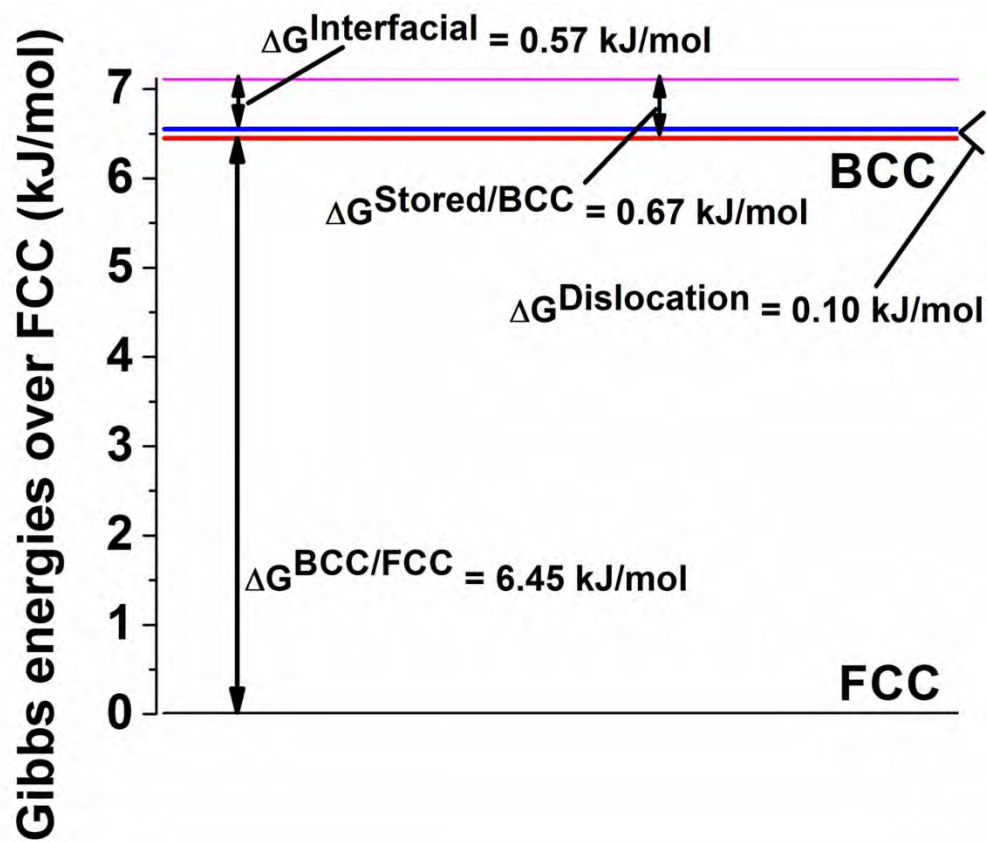
Fig. 26 The Gibbs energies relative to FCC phase for Ni mole fraction 0.9, where Gibbs energy for FCC phase is regarded as a reference. The energy increases due to FCC-BCC transformation, dislocation and interfacial area are labeled. The total stored energy on BCC phase due to deformation is also labeled in the figure.
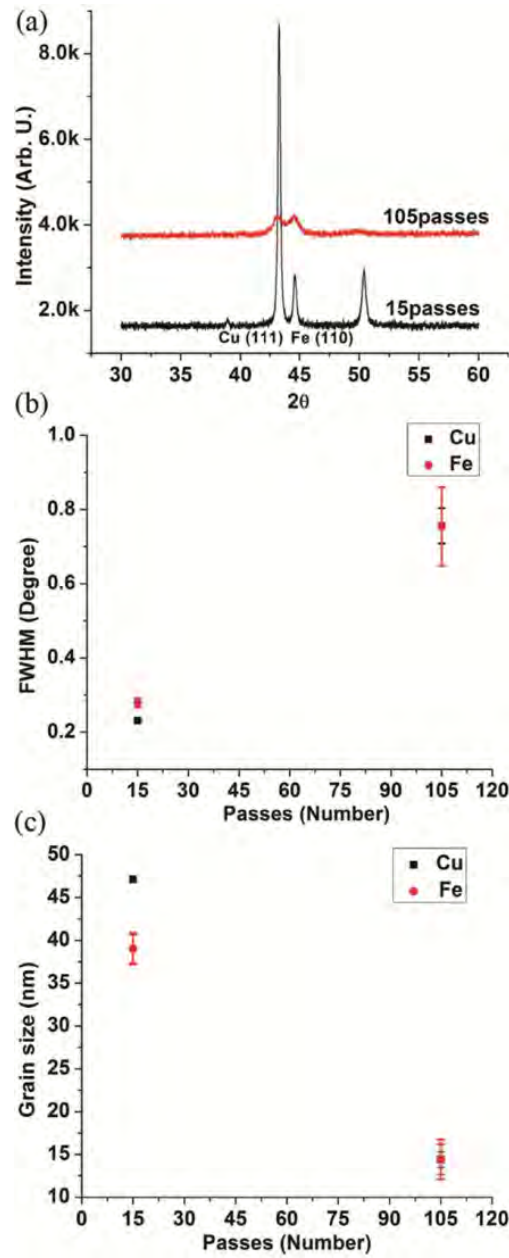
Fig. 27 (a) The XRD patterns of $Cu_{40}Fe_{60}$ multilayers sample after 15 and 105 passes. (b) The full width at half maximum of the XRD peaks. (c) The grain sizes estimated from Scherrer's formula.
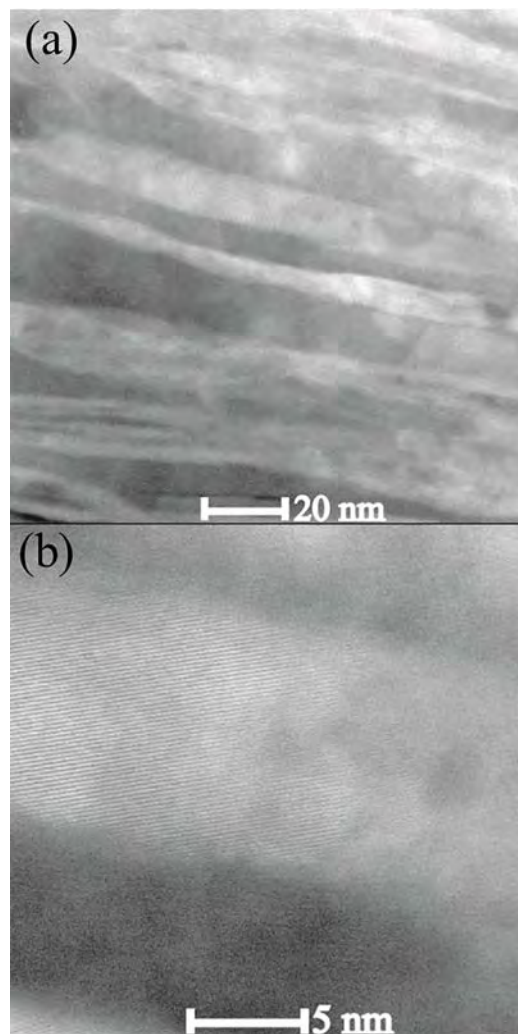
Fig. 28 (a) STEM image showing the Cu-Fe multilayer structure. Bright layer corresponds to Cu and dark layer corresponding to Fe. (b) High resolution STEM image showing the layer thickness and the grain shape. All images were taken by HAADF detector.
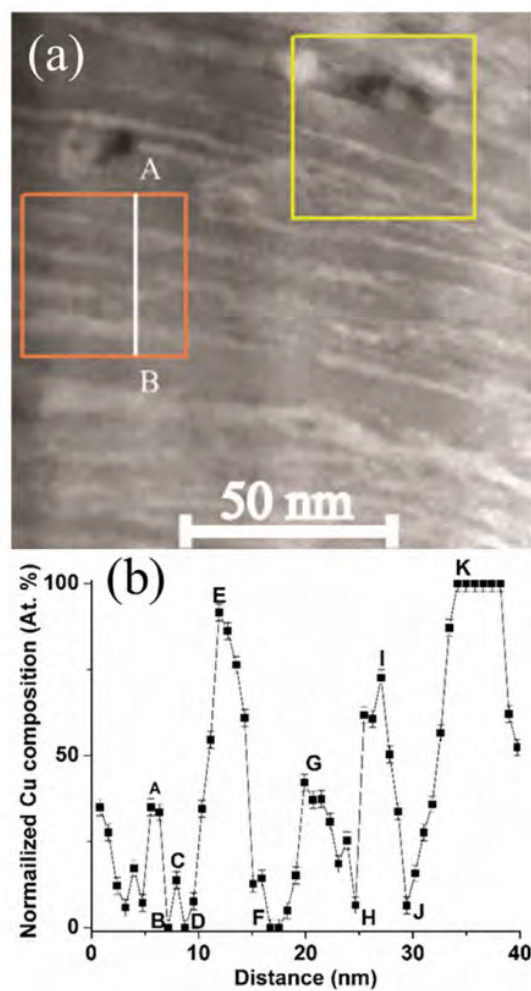
Fig. 29 (a) STEM image of the Cu-Fe multilayer structure. The orange box shows the region of interest where the drift-correction EELS image was taken. (b) The composition profile across the multilayers from A to B in (a). Letter A to K mark the characteristic positions in the composition profile.
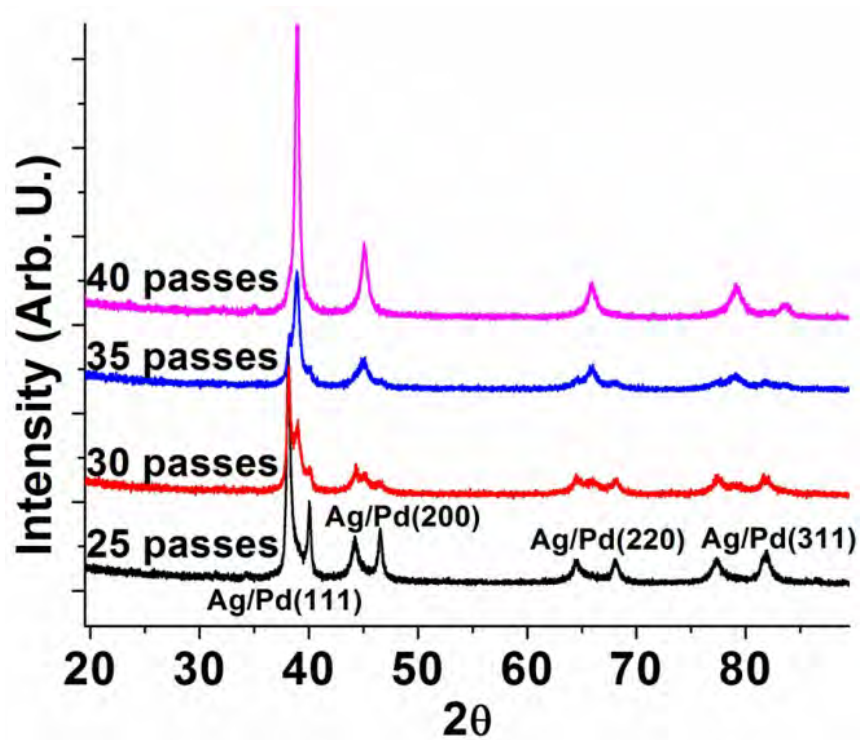
Fig. 30 XRD patterns for Ag60/Pd40 multilayer samples after 25, 30, 35 and 40 passes. The indices of different diffraction peaks are labeled in the figure.
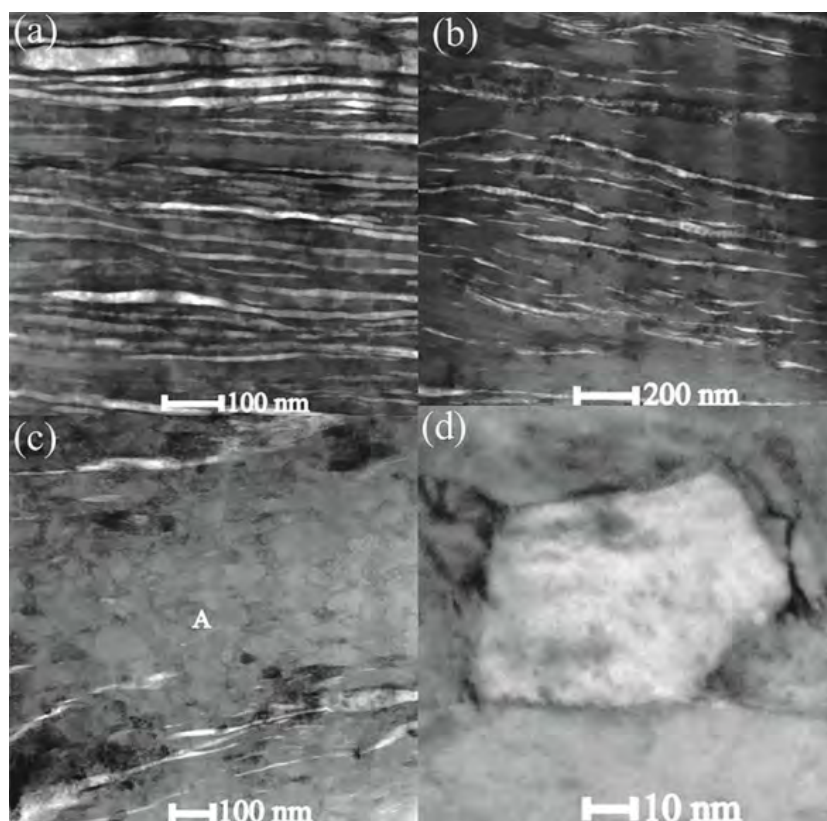
Fig. 31 (a) STEM cross-section image of Ag60/Pd40 muiltilayers after 25 passes (b) STEM cross-section image of Ag60/Pd40 muiltilayers after 30 passes. (c) STEM image of Ag60/Pd40 muiltilayers after 35 passes.The mark A is the position where EDX were taken. (d) A high magnification image of Ag60/Pd40 muiltilayers after 35 passes showing equiaxed grain structure. All images were taken by BF/DF detector.
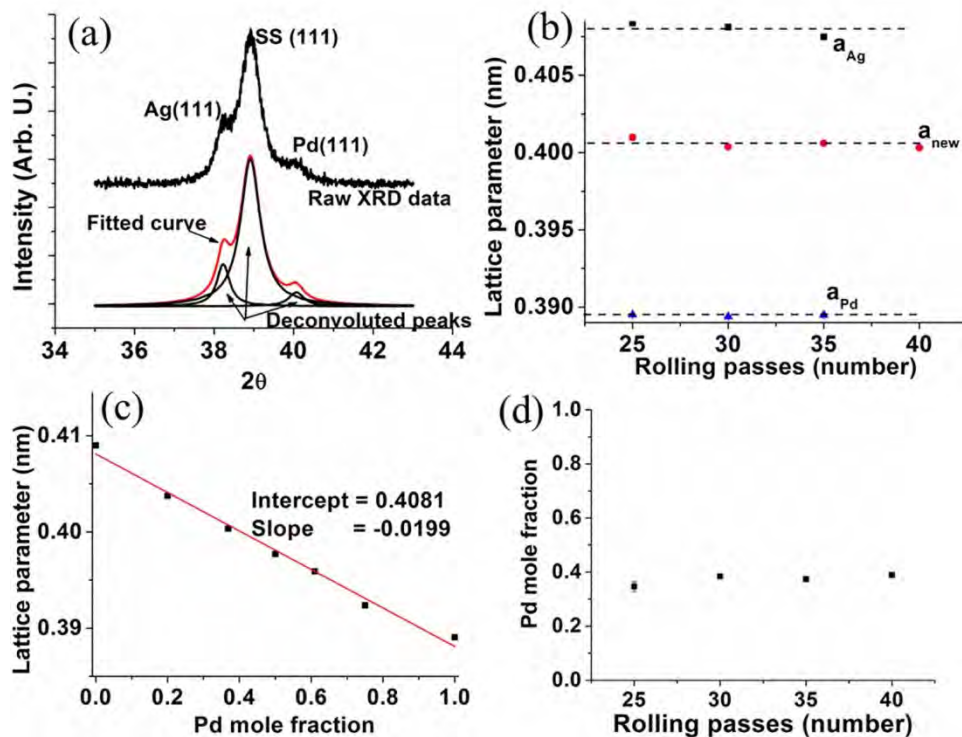
Fig. 32 (a) XRD raw pattern, fitted curve and deconvoluted peaks for multilayer sample after 35 passes. (b) Lattice parameters obtained by using deconvoluted peak positions and applying Bragg's law. (c) The linear fitting of lattice parameters of Ag-Pd solid solution against different Pd compositions. Data used for fitting in (c) is from Ref. 10. (d) The Pd compositions in the solid solution calculated by using the lattice parameters in (b) and applying the linear relationship between lattice parameter and Pd composition in (c).
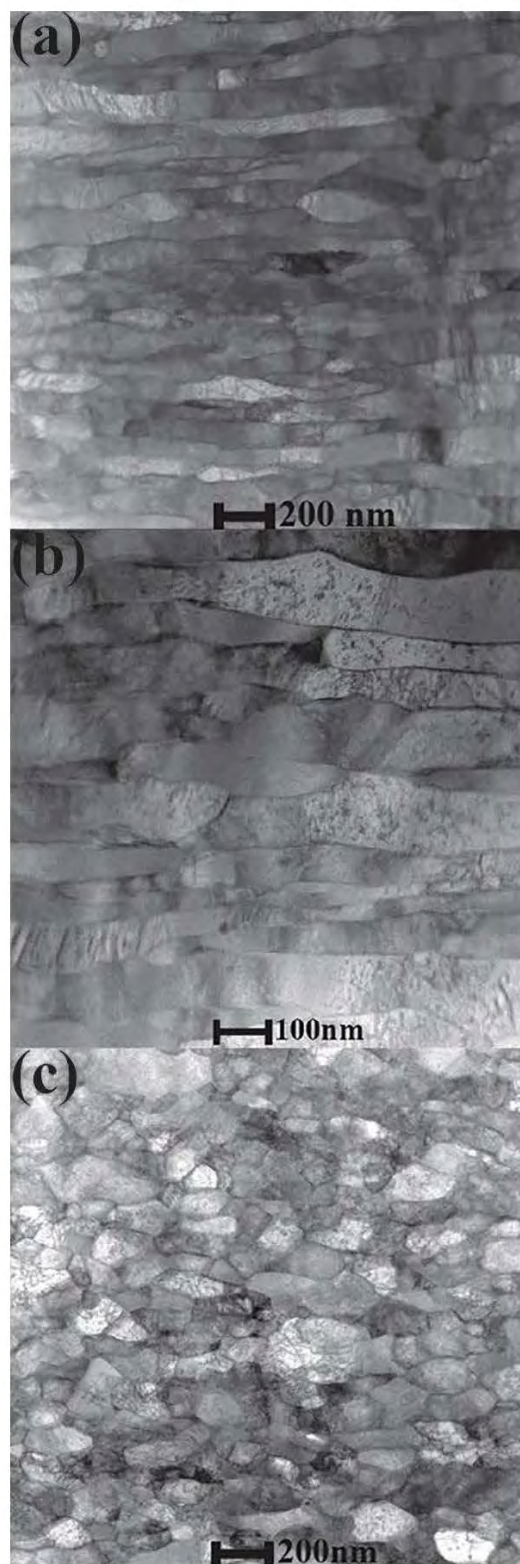
Fig. 33 (a) STEM cross-section image of monometallic Pd after 20 passes. (b) STEM cross-section image of monometallic Pd after 20 passes with a higher magnification. (c) STEM cross-section image of monometallic Pd after 40 passes.